



GPU-based, parallel-line, omni-directional integration of measured pressure gradient field to obtain the 3D pressure distribution

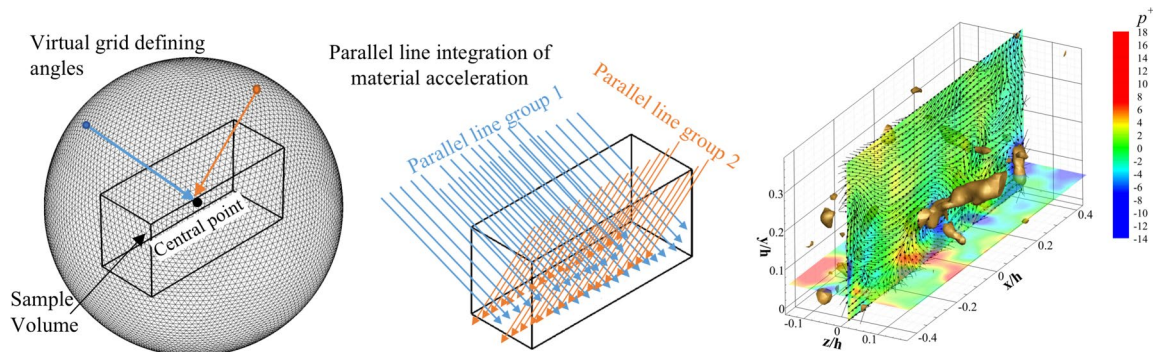
Jin Wang¹ · Cao Zhang^{1,2} · Joseph Katz¹

Received: 31 August 2018 / Revised: 21 December 2018 / Accepted: 12 February 2019
© Springer-Verlag GmbH Germany, part of Springer Nature 2019

Abstract

The introduction of 3D time-resolved velocity measurement techniques enables calculation of the instantaneous pressure distribution by spatially integrating the material acceleration. This paper introduces an efficient method for 3D integration of the acceleration, which does not require prescribed Dirichlet boundary condition on one of the surfaces, minimizes the propagation of errors in acceleration, and can be easily utilized in flows with complex boundaries. This parallel-line, omni-directional integration procedure (Omni3D) calculates the pressure at every point by integration from all directions, while avoiding regions with large acceleration errors. To reduce the computational costs, the calculations are performed by a GPU-based algorithm, which determines the 3D pressure field from tomographic PIV data in 1 min. The accuracy of Omni3D is compared to that of several techniques, including procedures based on solving the Pressure Poisson Equation (PPE) with different Dirichlet boundary conditions. The error analysis is based on Direct Numerical Simulation (DNS) data for isotropic turbulence, synthetic 3D PIV images for turbulent channel flow generated from DNS data, and experimental data. It examines the effects of spatial resolution, propagation, and avoidance of embedded local errors, boundary conditions, method for calculating the velocity, as well as viscous and sub-grid stresses on the calculated pressures. For acceleration fields with low errors and properly specified boundary conditions, Omni3D and PPE give similar results. However, Omni3D is more effective in suppressing the effects of acceleration errors. Sample experimental results including instantaneous plot of pressure, pressure statistics, and pressure–velocity correlations based on tomographic PIV data are also provided.

Graphical abstract



1 Introduction

✉ Joseph Katz
katz@jhu.edu

¹ Department of Mechanical Engineering, Johns Hopkins University, Baltimore, MD 21218, USA

² Simerics, Inc, Novi, MI 48375, USA

Knowledge about pressure distribution in a flow field is of vital importance in a variety of engineering problems, e.g., determining the lift force in airplane aerodynamics, and prediction of propeller performance and cavitation in marine hydrodynamics. Wall pressure fluctuations also play

a primary role in generation of flow-induced vibration and noise (Willmarth 1975; Bull 1996; Blake 2017). Furthermore, one of the unresolved challenges in modelling of high Reynolds number turbulent shear flows involves the pressure–velocity correlations in the Reynolds stress transport equations (Batchelor 1951; Corcos 1963; Pope 2000; Liu and Katz 2017). The classical method for pressure-based force measurement involves integration of the surface pressure distribution based on data obtained at discrete point pressure taps or pressure sensitive paints (PSP) (Sexton et al. 1973; Peterson and Fitzgerald 1980; Morris 1995; Bukov et al. 1992). However, with the introduction of particle image velocimetry (PIV)-based techniques, recent unsteady force measurements on a rotary wing already involve calculation of the pressure distribution from the time-resolved velocity field, followed by spatial integration over the surface (Villegas and Diez 2014). Likewise, while most of the present experimental data on pressure fluctuations in turbulent flow away from boundaries have been obtained using inserted probes (e.g., Tsuji and Ishihara 2003; Tsuji et al. 2007), recent studies have transitioned to PIV-based techniques. Several approaches have been used, including direct integration of material acceleration (Liu and Katz 2006; Joshi et al. 2014; Zhang et al. 2017), solving the pressure Poisson equation (PPE) (e.g., Roache 1976; de Kat and van Oudheusden 2012; van Oudheusden 2013), and integration in the Fourier domain (Huhn et al. 2016). Methods relying on time-resolved particle tracking velocimetry (PTV) data, such as Shake-The-Box (Schanz et al. 2016), to obtain the acceleration, and then integrating it using PPE on the unstructured grid have also been introduced (van Gent et al. 2017).

Considerable effort has already been invested to determine the uncertainty in the material acceleration by Eulerian or Lagrangian method (Lynch and Scarano 2014; de Kat and van Oudheusden 2012) as summarized in recent review papers (van Oudheusden 2013). In general, the conclusion of these studies is that the Lagrangian approach is less sensitive to errors in velocity (Violato et al. 2011). Recently introduced techniques to increase the accuracy of the Lagrangian approach include fluid trajectory correction (Lynch and Scarano 2013, 2014) and ensemble-averaged correlation (Jeon et al. 2014). For planar pressure reconstruction, solving the PPE is the popular approach (Villegas and Diez 2014; van Oudheusden et al. 2007; Violato et al. 2011; Schneiders et al. 2016; Jeon et al. 2016; Tronchin et al. 2015). Direct planar integration of instantaneous material acceleration has been reported initially by (Baur and Köngeter 1999) where the integration is performed along four equally distributed paths. Since the limited number of paths carry with them cumulative effects of local acceleration errors, Liu and Katz (2006, 2013) have introduced the 2D virtual boundary omni-directional integration method (Omni2D) and its latest version of rotating-ray

omni-directional integration (Liu et al. 2016). It determined the pressure at each point by integration along all directions originating from equally separated points along a virtual circle surrounding the sample area. This approach prevents local-path clustering, especially near boundaries, and minimizes the propagation of errors from regions with high acceleration errors. This method has already been used to calculate pressure in turbulent boundary layers (Joshi et al. 2014) and cavity shear layers (Liu and Katz 2013, 2017). Using synthetic data for comparing integration methods, Charonko et al. (2010) conclude that PPE performs better for Poiseuille flow and Omni2D is better for a vortex.

While PPE can be readily extended to volumetric measurements using, e.g., time-resolved tomographic PIV data (Elsinga et al. 2005; Ghaemi et al. 2012; Ghaemi and Scarano 2013), extension of Omni2D to 3D, has been problematic owing to the massive amount of computations involved. Yet, as discussed in this paper, omni-directional integration is effective in minimizing the impact of local acceleration errors, and provides a convenient means of avoiding areas with high acceleration errors. Hence, the goal of the present effort is to develop and evaluate a fast and robust 3D pressure reconstruction method based on similar principles. The new GPU-based, parallel-line, 3D omni-directional method (Omni3D) discussed in the next section integrates the material acceleration along a series of parallel lines aligned in all possible directions. The pressure at every point is the average value obtained from integration along all the paths crossing this point. Hence, errors associated with a certain path are minimized. Iterations, typically 3–4, are used for correcting the initially assumed pressure distribution along the external surfaces of the sample volume. Hence, there is no need to prescribe a pressure distribution along the boundary. Methods for identifying and avoiding regions with particularly high material acceleration errors are also introduced and verified. In Sect. 3, the new technique is evaluated using forced isotropic turbulence data and synthetic 3D PIV data generated from results of Direct Numerical Simulations (DNS) for turbulent channel flow. The analysis examines the propagation of errors, and effects of spatial resolution on the pressure distributions for several integration approaches, including the more commonly used PPE method with different boundary conditions. Samples of applications using experimental data are provided in Sect. 4.

2 GPU-based, 3D parallel-line, omni-directional integration (Omni3D)

For an incompressible flow field with velocity $\mathbf{u}(\mathbf{x}, t)$, the 3D instantaneous pressure field can be obtained by integrating the Navier Stokes Eqn:

$$\frac{D\mathbf{u}}{Dt} = -\frac{1}{\rho} \nabla p + \nu \nabla^2 \mathbf{u} \quad (1)$$

where D/Dt denotes the material derivative, and boldface denotes a vector. The viscous term is usually neglected away from boundaries at high Reynolds numbers, but should be evaluated and included in the analysis in specific regions. For pressure reconstruction using Omni3D, groups of parallel lines covering the entire sample volume and aligned along all possible directions are used for defining the integration paths. Integration steps proceed from node to node which has the minimal distance from the straight line defined by the angle and end points. This process is referred to as parallel line omni-directional integration (PLODI) procedure in subsequent discussions. As the initial step, iterations (typically 3–4) are used for determining the pressure distribution along the boundaries that is consistent with the internal acceleration field. The first iteration uses a selected pressure distribution along each boundary using, e.g., Omni2D. Different boundary planes are connected initially by matching the pressure in one of the common points, resulting in discontinuities in other points. These discontinuities are corrected/eliminated by the iterations and do not have any effect on the final converged pressure distribution. Then, the PLODI is applied to calculate the pressure difference between boundary points (only). The results of integration from all directions are averaged to provide an updated pressure in each boundary point. This procedure is subsequently repeated until the data converges, i.e., the pressure distributions along the surfaces are consistent with the internal 3D acceleration field. In the next step, PLODI is applied to compute the pressure in the inner nodes as well based on the converged pressure distribution along the boundaries.

The pressure in each internal point is the average of values obtained from all integration paths that start in boundary nodes and end at this point. This averaging is aimed at minimizing the impact of propagation of random errors in acceleration along the integration paths. Computations of the internal pressure do not involve iterations.

The purpose of performing the integration along groups of parallel-line oriented in different directions is to improve the efficiency of the computations in comparison to the original Omni2D (Liu and Katz 2006, 2008, 2013; Liu et al. 2016). The two parameters for generating the parallel lines are the angle/orientation and the line spacing. As illustrated in Fig. 1, the angles are defined by connecting nodes distributed uniformly on a spherical virtual grid surrounding the sample volume to the center of the sphere. This uniform spherical grid assures that the integration angles are distributed homogeneously. In general, there are only five regular polyhedrons that can equally divide a sphere and generate a strictly uniform spherical grid, namely a tetrahedron, cube, octahedron, dodecahedron and icosahedron, but the associated number of vertices is not large enough to satisfy the required resolution. To create a dense homogeneous grid, an initial icosahedron grid is divided recursively multiple times. In every step, the triangular surface is divided into four equal parts, and then projected onto the surface of the sphere. Repeating this procedure six times generates a spherical triangular grid with 20,480 faces (Fig. 1a). This procedure is only used for defining the angles. The integrations by PLODI are performed from boundary to boundary nodes

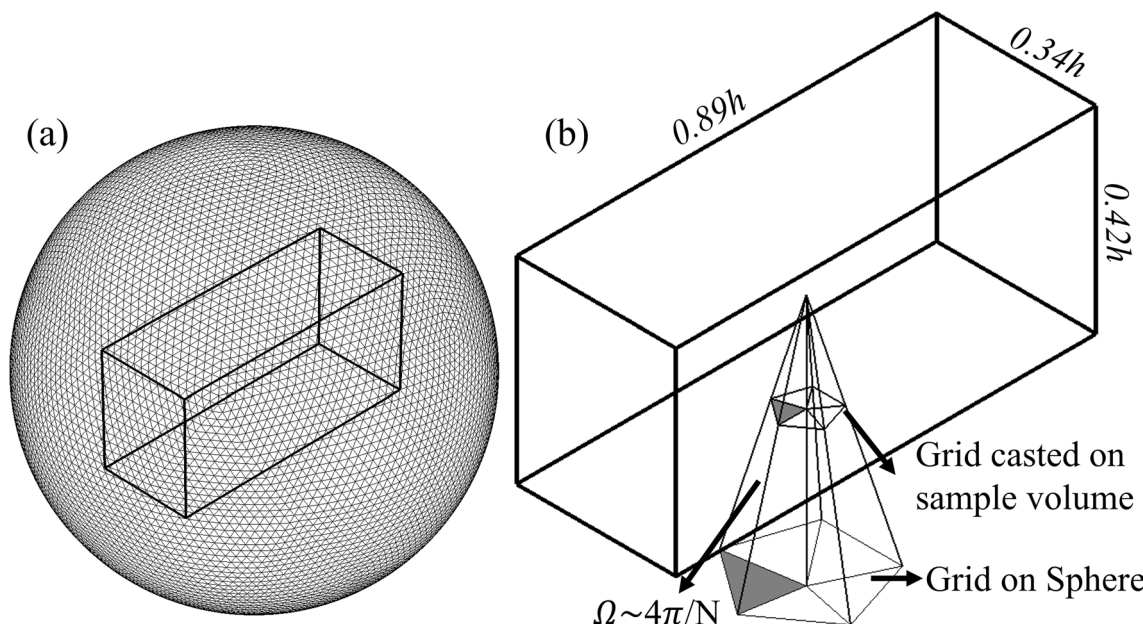


Fig. 1 **a** The grid with 10,242 points, and 20,480 triangular surfaces used for generating the directions of the parallel line integration paths, and **b** matching the resolution of the virtual spherical grid with that of the experimental grid on the surface of the sample volume

along parallel lines. The distance between these lines is a free parameter.

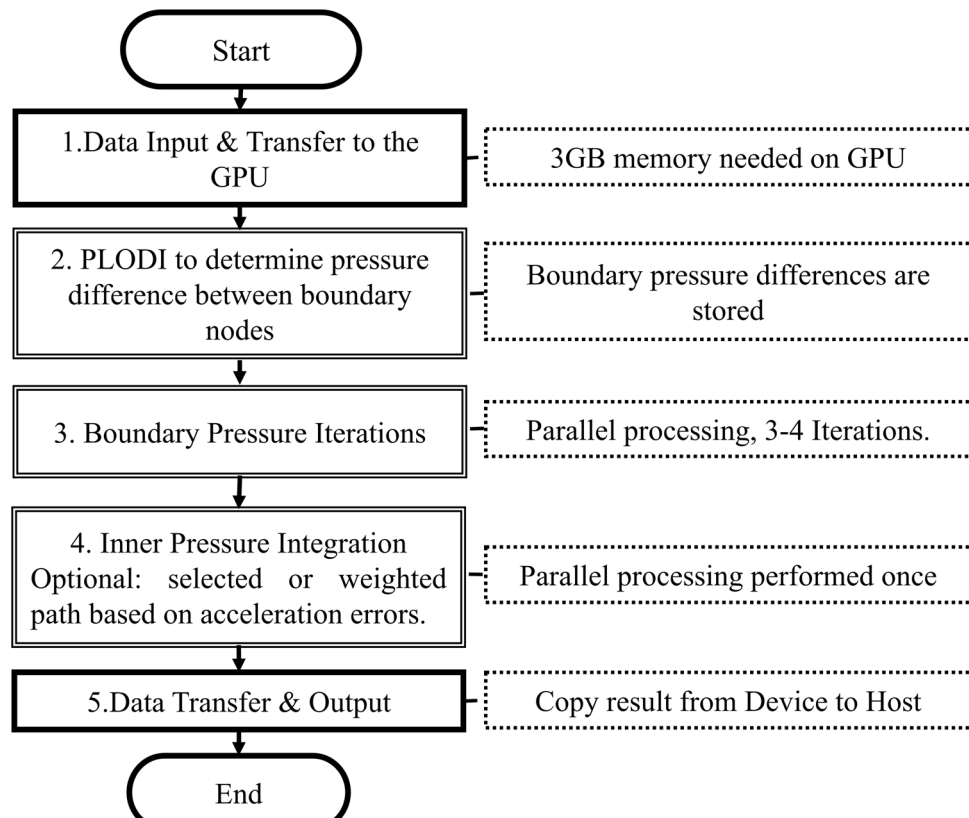
The following discussion addresses the size of the integration grid and computation time. The grid on the spherical virtual boundary should be dense enough to match the data within the sample volume. For N surface triangles on the sphere, the average solid angle of each triangle is $\Omega = 4\pi/N$. The projected area of this triangle on the boundary of the sample volume is about $4\pi(L/2)^2/N$, where L is the corresponding length. To match this projected area with the characteristic resolution of the PIV data (denoted as Δx), $4\pi(L/2)^2/N \sim 0.5\Delta x^2$, where the 0.5 factor accounts for the area ratio between a triangle and a square. Hence, $N \sim 2\pi(L/\Delta x)^2$. For example, for a data grid of $100 \times 47 \times 38$ velocity vectors obtained in recent tomographic PIV measurements (Zhang et al. 2015, 2017), using $L/\Delta x \sim 70$ (diameter of an equivalent sphere) gives $N \sim 3 \times 10^4$. The actual number of faces used in our calculations is 20,480. The implications as far as the amount of computation involved are as follows: suppose M is the number of angles defined by the spherical virtual grid and Δ_{LS} is the spacing between parallel lines. Then, the total number of integration paths is about $M(L/\Delta_{LS})^2$. For the above-mentioned icosahedron-based grid, according to Euler's formula (Spanier 1966), $N + M - E = 2$, where E is the total number of edges. Since each edge is part of two surfaces, for triangles, $E = 3N/2$, giving $N = 2(M - 2)$, i.e., $M = 10,242$. Choosing $\Delta_{LS} \sim \Delta x$, the number of integration

paths is in the order of 10^8 . Consequently, it takes more than 3 h for integrating the acceleration in a single $100 \times 47 \times 38$ voxel grid using a C++-based code running on a quad-core, 3.7 GHz Intel i7-3860 processor. Considering that only the original acceleration data are read and integrated along a single path, the integrations along different lines are independent of each other, i.e., they do not require any communication among them. Hence, the algorithm can be readily optimized for parallel computing using a GPU system. The flow chart for the parallel computation developed for this purpose is presented in Fig. 2. It consists of the five steps:

- (i) Allocation of memory on the GPU device, as well as reading and transferring of the acceleration data to the GPU memory.
- (ii) Using PLODI in parallel to obtain the pressure difference between each two boundary nodes, denoted as $PINT(n_{in}, n_{out})$, where, n_{in} and n_{out} are the starting and ending points of an integration path.
- (iii) Calculating the pressure in each of the boundary nodes by averaging the results of integrations from all directions. This step is performed using

$$P_{n_{out}}^{\text{new}} = \frac{\sum_{n_{in}=1, n_{in} \neq n_{out}}^{N_{\text{surface}}} (P_{n_{in}}^{\text{old}} + PINT(n_{in}, n_{out}))}{N_{\text{surface}} - 1}, \quad (2)$$

Fig. 2 Flow chart (solid lines) and notes (dotted lines) for the Omni3D integration of acceleration. Double-lines indicate processes running on the GPU board, and single lines, processes run on the CPU



where N_{surface} is the total number of grid points on the surface of the sample volume. The values of M or N could be selected independent of N_{surface} . Theoretically, for large line spacing and small number of angles, some boundary points could be missed. As a rigorous error analysis later in this paper shows, such occurrence is undesirable in the application of Omni3D, and that the optimal line spacing is comparable to the grid spacing. After updating the pressure over the entire surface, this procedure is repeated until results converge. Typically, 3–4 iterations are sufficient to reach convergence.

- (iv) Inner pressure integration: in parallel, each GPU thread is assigned an integration path from boundary to boundary nodes, and PLODI is applied to calculate and store the pressure in inner nodes along this path. The value obtained by averaging the results obtained for all the paths is the final pressure in each internal node.
- (v) Transferring the data from the GPU to the host memory and storing it.

The timeline for applying the Omni3D method in the $100 \times 47 \times 38$ voxel grid is shown in Fig. 3. As is evident, using a low-cost, Tesla K40c GPU board, which has 2880,745 MHz processors and 12 GB memory, reduces the

total computation time to about 1 minute. The data transfer and memory allocation take 16 s; calculating the pressure difference between boundary nodes costs 15 s; parallel iterations to obtain the pressure along the boundary takes 10 s; and calculating the internal pressure costs 20 s. Furthermore, as recent tests have shown, using an advanced GPU Geforce RTX 2080 Ti board and the newer Cuda 8.0 toolkit, reduces the computation time of Omni3D by 6 times, to about 10 s. The pressure increments between boundary nodes are stored in the global memory of the GPU board to save the data transfer time. Consequently, only two applications of PLODI are needed to obtain a converged pressure field, one for the surface values, and the other for internal points. A modified approach, which would maintain the internal pressure differences between nodes during the initial application in step 2 could reduce it to one; however, it requires much larger amount of memory. The current approach is 180 times faster than pressure calculations using the above-mentioned CPU. Currently, all the computations are performed in single precision (32 bit), for which the peak floating-point performance of the present GPU is 4.29 Tflops. Using double precision, this performance decreases to 1.43 Tflops, causing an increase in computation time to about 3 min. The computation time can be further reduced by implementation of kernels concurrency as well as concurrency between memory

Fig. 3 Timeline in seconds for application the Omni3D method on the Tesla K40c GPU processor for a $100 \times 47 \times 38$ voxel grid

		Timelines (s):					
		10	20	30	40	50	60
On CPU	Memory Allocation	6					
	Reading Acceleration						
	Copying Data from host to GPU						
	Copying Data from GPU to Host						10
	Storing the pressure data						
On Tesla K40c GPU	Calculating the pressure difference between boundary points		15				
	Iteratively calculating the pressure distribution along the boundaries			10			
	Calculating the internal pressure distributions				20		
Step No. :		1	2	3	4	5	

copying and kernels when the code is used to compute a time series of the pressure field.

3 Evaluation of the pressure measurement tools using DNS data

Direct numerical simulations (DNS) data for forced isotropic turbulence and turbulent channel flow obtained from the JHU DNS database (Li et al. 2008; Perlman et al. 2007) have been utilized for comparing the Omni3D procedure with other methods, including Omni2D and PPE with different approaches for determining the boundary conditions. The analysis involving forced isotropic turbulence compares: (i) the errors in pressure during integration of the DNS acceleration by the various techniques; (ii) the impact of introducing randomly distributed errors in acceleration in part of the flow field on the pressure in other sections and (iii) the impact of unresolved sub-grid turbulence on the pressure distribution. The channel flow DNS data is used for generating and then translating synthetic particle fields, which are then analyzed at varying resolution and approaches to obtain the corresponding velocity, acceleration, and pressure fields. Comparisons to the DNS results are used for: (i) determining the effect of the spatial resolution of the data, (ii) the effects of boundary conditions used during the analysis, (iii) the impact of regions with elevated acceleration errors on the pressure, and (vi) improvements achieved by avoiding zones with errors exceeding prescribed values.

3.1 Analysis based on isotropic turbulence data

3.1.1 Effects of boundary conditions and integration method

Velocity, pressure, and terms used for forcing the turbulence (denoted as f) for a $64 \times 64 \times 64$ grid are fetched from the JHU database. The distribution of material acceleration is calculated by Lagrangian tracking of imaginary particles with zero size. These virtual particles are placed on a regular grid at time t , and then tracked forward and backward in time. Their subsequent positions are calculated by solving

$$\frac{Dx_p}{Dt}(x(t), t) = u_p(x(t), t), \quad (3)$$

where x_p and u_p are the particle location and velocity, respectively, using second-order accurate Runge–Kutta integration (Yu et al. 2012) with time step equal to the temporal resolution of the DNS data. Results are interpolated onto the original DNS grid using 6th order Lagrangian interpolation. The material acceleration is obtained using

$$\frac{Du_p}{Dt}(x(t), t) = \frac{u_p(x(t + n\Delta t), t + n\Delta t) - u_p(x(t - n\Delta t), t - n\Delta t)}{2n\Delta t}, \quad (4)$$

for $n = 1, 2$, and 3 and averaging them, neglecting the viscous terms, and accounting for the forcing, $\nabla p = -\frac{Du_p}{Dt} + f$, with the latter being available from the database. Neglecting the forcing term would cause significant errors to pressure, as shown before in Liu and Katz (2006). Four different methods for integrating ∇p are implemented to obtain the pressure:

- (i) The previously described Omni3D.
- (ii) Planar integration using Omni2D (Liu and Katz 2006, 2013) in a series of planes. However, the accelerations used are two components of 3D acceleration, accounting for out-of-plane velocity. They are then matched by applying the same procedure in a selected central perpendicular plane. The pressure distribution along the line intersecting each of the original planes is then averaged to obtain the constant needed for matching this plane with the others.
- (iii) Solving PPE

$$\nabla^2 p = -\rho \nabla \cdot \frac{Du}{Dt}, \quad (5)$$

with Dirichlet boundary condition (BC) on one surface and Neumann (∇p) in the others. The source term is obtained by taking the divergence of the above-mentioned material acceleration.

Prior studies have shown that erroneous data originating from the Dirichlet boundary conditions are significant contributors to errors in the bulk pressure, especially near the boundary (Ghaemi et al. 2012). To reduce this effect, Omni2D is used for determining the pressure distribution along the Dirichlet boundary. Hence, this approach is referred to as PPE-Omni2D in subsequent discussions. The integration is performed iteratively using a Jacobi Poisson solver with second-order central difference discretization.

$$p_{i,j,k}^{n+1} = \frac{p_{i+1,j,k} + p_{i-1,j,k} + p_{i,j+1,k} + p_{i,j-1,k} + p_{i,j,k+1} + p_{i,j,k-1}}{8} + \frac{1}{8} \rho \Delta x^2 (\nabla \cdot \frac{Du}{Dt})_{i,j,k}, \quad (6)$$

as done in a series of recent papers (e.g., Ghaemi et al. 2012; Ghaemi and Scarano 2013; Villegas and Diez 2014). The convergence criterion is the difference between results of successive iterations of less than $1e-13$. To achieve such convergence, the typical number of iterations is 50,000.

- (i) Solving PPE with Dirichlet BC on one surface and Neumann on the others. Following de Kat and van

Oudheusden (2012), the Dirichlet BC is estimated using Bernoulli's Equation.

$$p_{\text{ref}} - p' = \frac{1}{2} \rho (u'^2 + v'^2 + w'^2) = \text{TKE}, \quad (7)$$

where (u', v', w') are the velocity fluctuation ($u_i = U_i + u'_i$) components in the (x, y, z) directions, respectively, p' is the pressure fluctuation, and p_{ref} is a constant reference pressure needed for the integration. For the DNS data, p_{ref} can be obtained from the database. This approach is referred to in this paper as PPE-Ber1. Note that for the isotropic turbulence data of the JHU DNS database, $p'_{\text{RMS}}/\text{TKE} = 0.5$. Another approach,

$$p - p_\infty = \frac{1}{2} \rho (U_\infty^2 - U^2), \quad (8)$$

has been proposed by Ghaemi et al. (2012), Ghaemi and Scarano (2013) for boundary layer flows. Here p is the value used for the boundary condition; p_∞ and U_∞^2 are reference pressures and velocity, respectively; and U^2 is the instantaneous local streamwise velocity component (squared). They show that the impact of errors introduced by these boundary conditions diminishes with increasing distance from this boundary. For example, it has a small effect on the wall pressure fluctuations if the Dirichlet BC is imposed in a wall-parallel surface located 0.2δ from the wall, where δ is the boundary layer thickness. This approach is referred to as PPE-Ber2 in the discussion about channel flows.

For all the pressure fields obtained using the above-mentioned methods, the spatially averaged pressure over the entire volume, which is used as a reference pressure, is set to zero. The same applies to the DNS data. Sample instantaneous pressure distributions comparing the computed pressure (p) to the original DNS pressure (p_{DNS}), and the associated scaled errors ($p_{\text{DNS}} - p$)/TKE are presented in the first and second rows of Fig. 4, respectively. The various Dirichlet BCs are imposed at $y/L = 0.28$, where L denotes the DNS integral scale. A plot showing the Root-Mean-Square (RMS) of scaled error for each y averaged over 100 samples (time steps) is presented in Fig. 4j. The Probability Density Functions (PDFs) of errors over the entire volume of 100 realizations for the various conditions are shown in Fig. 4k, l in linear and log scales, respectively. Since results averaged over the 100 realizations display very similar trends to those observed in individual realization (not shown), the rest of the analysis performed in this section (isotropic turbulence) is based on characterizing the errors in a selected single realization. As is evident, all the instantaneous pressure distributions appear to be similar (Fig. 4a–d), but the errors differ substantially (Fig. 4e–h). The pressure and error

distributions for the Omni3D (Fig. 4a, e) and PPE-Omni2D (Fig. 4c, g) are very similar to each other, but the PDFs indicate that Omni3D has lower errors. The error distribution (Fig. 4g) and RMS value for the Omni2D method are significantly higher than those of Omni3D and PPE-Omni2D over the entire field of view. Examination of the data (not shown here) indicates that it is caused by inadequate matching of planes. Implementation of PPE-Ber1 causes a 0.26 error in the Dirichlet boundary, as expected, but it decreases to 0.01 on the opposite boundary. Evidently applying Omni2D to calculate the Dirichlet BC in applications involving PPE reduces the error substantially over the entire field of view. Another potential alternative method is to specify a Dirichlet boundary condition in a limited number of points, as done by Jeon et al. (2016) and Violato et al. (2011), or presumably, even a single Dirichlet point (PPE-PD). Sample tests performed for a single Dirichlet point display trends that are similar to those of PPE-Omni2D.

3.1.2 Error propagation

To examine the propagation of errors in acceleration, expected to occur in PIV data, randomly distributed errors with maximum value of $3\sqrt{p_{\text{max}}}$ are added to the DNS acceleration field in 10 x - y planes located at the center of the sample volume ($0.12 < z/L < 0.16$). A y - z plane view of the local error distribution for the Omni3D method is presented in Fig. 5a. Results for the PPE-Omni2D approach with the Dirichlet BC applied on the $y/L = 0.28$ surface are shown in Fig. 5b. The errors for PPE-Omni2D with the Dirichlet BC imposed at $z/L = 0.28$ are presented in Fig. 5c. In all cases, the errors propagate into the regions with no acceleration errors. Results for Omni3D are very similar to those of PPE-Omni2D on the Dirichlet surface located far from the region with high acceleration error (Fig. 5c). However, when the region with imposed errors is adjacent to the Dirichlet surface (Fig. 5b), the errors near this surface are noticeably higher, mostly since the imposed errors contaminate the boundary condition. Corresponding profiles of RMS errors spatially averaged over x - y planes are plotted in Fig. 6. Figure 6a shows the profile for Block A marked in Fig. 5b, i.e., far from the Dirichlet boundary, and Fig. 6b presents the results for block B, namely near the Dirichlet boundary. As is evident, away from the Dirichlet boundary, the PPE-Omni2D and Omni3D results share the similar error profiles. However, there is clear difference near the Dirichlet boundary, where the error propagation of the PPE pressure is significantly higher than that of the Omni3D results. If the same comparison is performed using the PPE-Ber1 procedure, the error near the Dirichlet boundary is orders of magnitude higher.

Next, the mechanism of error propagation in the Omni3D integration is elucidated theoretically using a simplified

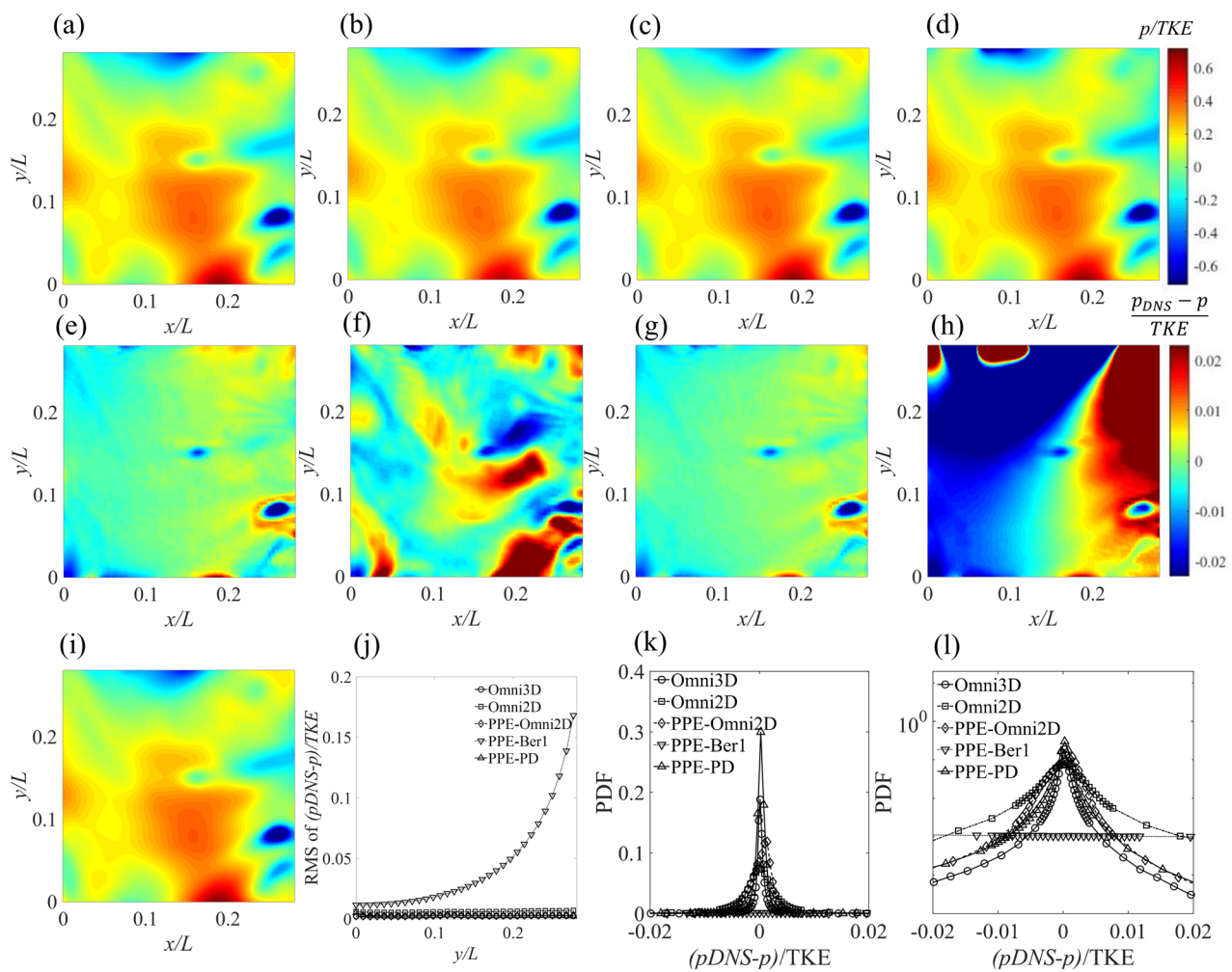


Fig. 4 First row: instantaneous pressure distribution calculated using DNS data of forced isotropic turbulence (shown in **i**), and second row: the corresponding errors normalized by the turbulent kinetic energy (TKE). The methods used are: **a, e** 3D omni-directional integration, **b, f** 2D virtual boundary omni-directional integration, **c, g**

solving PPE with Omni2D BC, and **d, h** solving PPE with Bernoulli (Ber1) BC. **j** Variations in RMS error profile of pressure averaged over 100 samples. **k, l** PDF of error in pressure over 100 samples in linear scale and log scale

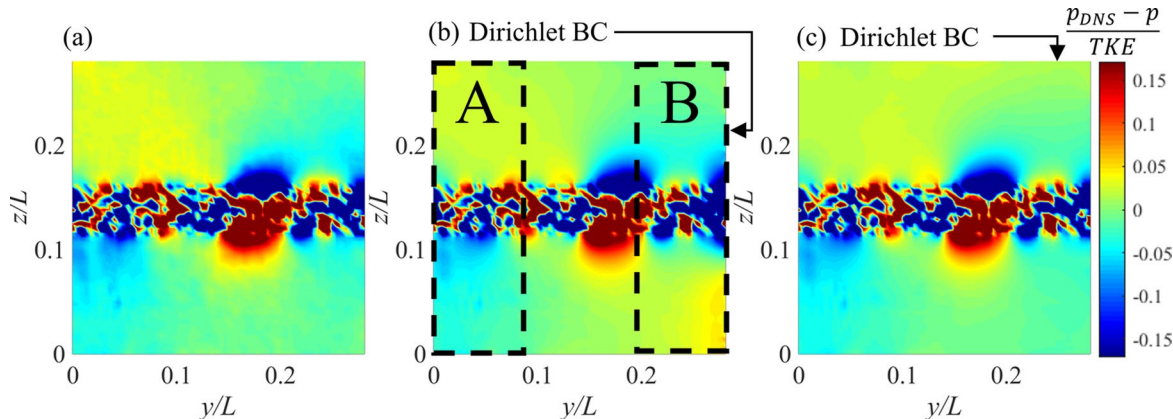


Fig. 5 A sample central plane showing the effect of embedding randomly distributed $\pm 300\%$ error in acceleration at $0.12 < z/L < 0.16$ on the pressure distribution in the isotropic turbulence. The pressure is

calculated using: **a** Omni3D, **b** PPE-Omni2D with Dirichlet BC on the $y/L = 0.28$ surface, and **c** PPE-Omni2D with Dirichlet boundary condition on the $z/L = 0.28$ surface

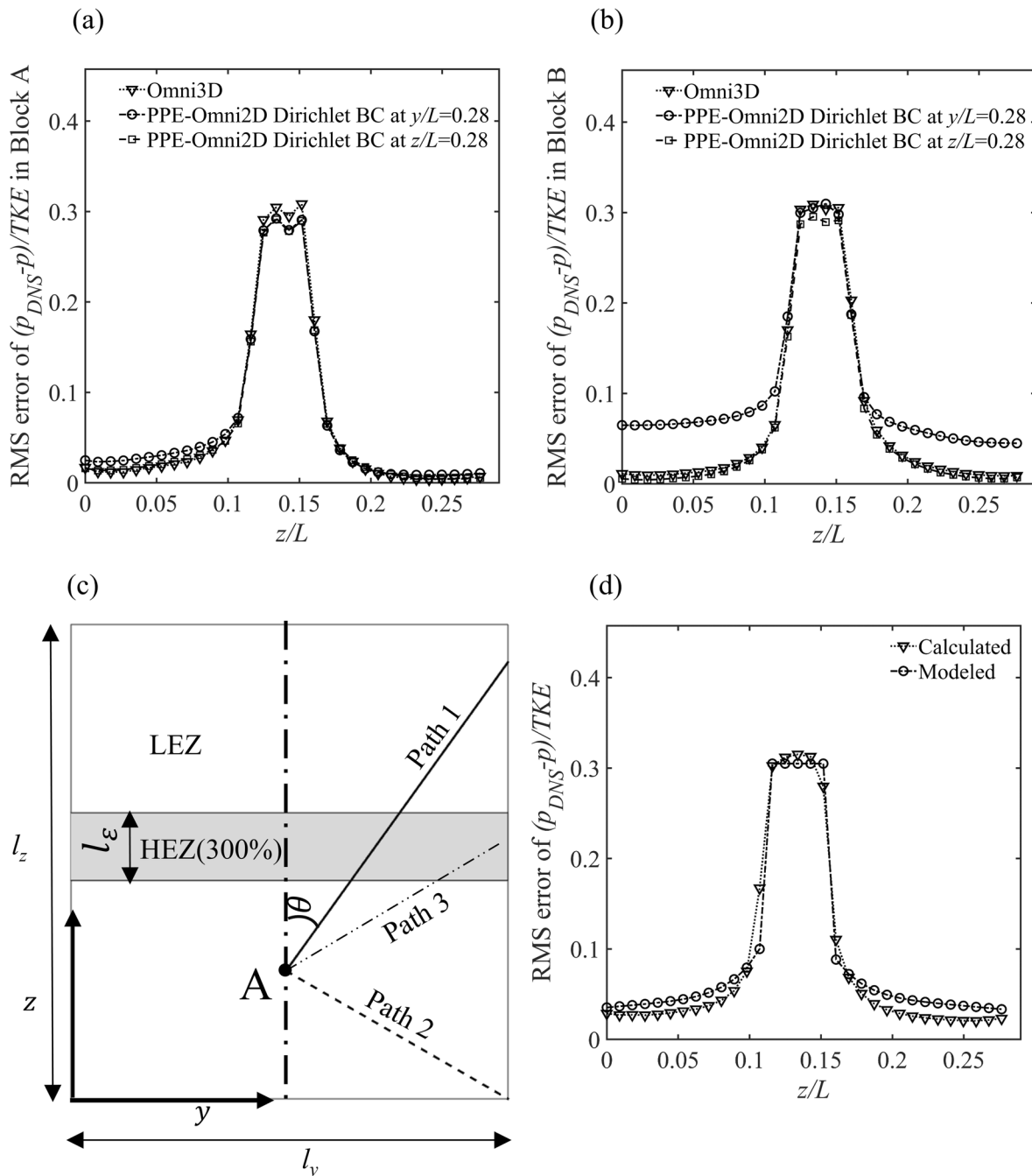


Fig. 6 Spatially averaged RMS error profiles over (x, y) planes of the isotropic turbulence with embedded error at $0.12 < z/L < 0.16$: **a** for block A in Fig. 5, and **b** for block B in Fig. 5. **c** Illustration of paths

dissecting the high error zone (HEZ) at different angles, and **d** a comparison between modeled and calculated error profiles

model. As illustrated in Fig. 6c, the domain is divided to high error zone (HEZ), where the acceleration error is 300%, and a low error zone (LEZ), where the error is negligible. Three different types of integration paths are considered, all of them starting from the boundaries and ending in point A, with two of them crossing the HEZ. Path 1 starts outside of HEZ and crosses it entirely. Path 3 starts inside this zone and

extends beyond it. Both are expected to contribute to the error in p_A . For each path, $p_A = p_{BC} - \rho \sum \left(\frac{Du}{Dt} \right)_i \cdot \Delta I_i$, with ΔI_i being the integration step, and p_{BC} is the pressure along the boundary. The uncertainty that this path introduces in point A, $(\varepsilon_p^2)_A$, can be estimated from $(\varepsilon_p^2)_A = \rho^2 \sum \varepsilon_{Du/Dt,i}^2 \Delta I_i^2$, where $\varepsilon_{Du/Dt}^2$ is the acceleration

error. Accordingly, the contribution to the error for a path 1 types is $l_e^2 \sec^2 \theta \epsilon_{Du/Dt}^2$, and for the path 3 type is $\rho^2 \left(\frac{l_y}{2} - \left(\frac{l_z}{2} - z_A - \frac{l_e}{2} \right) \tan \theta \right)^2 \csc^2 \theta \epsilon_{Du/Dt}^2$, considering the error carried is proportional to path length inside the HEZ and assuming uniform error distribution inside HEZ. The total error in point A is the average value obtained from all possible integration paths. The predicted RMS error profile averaged over all values of x and y is plotted and compared to the Omni3D results in Fig. 6d. The difference between them outside of the high error zone is less than 5%. These results demonstrate that the error propagation is predictable, and as demonstrated later, will guide the development of means to alleviate the impact of high-error regions.

3.1.3 Effect of sub-grid stresses

In addition to errors in velocity (discussed later) not resolving, the flow field down to the Kolmogorov scale introduces sub-grid scale (SGS) stress (Rogallo and Moin 1984; Lesieur and Métais 1996; Liu et al. 1994), $\tau = \tilde{u}\tilde{u} - \widetilde{u}\widetilde{u}$ into the momentum equation

$$\frac{\partial \tilde{u}}{\partial t} + \nabla \cdot \tilde{u}\tilde{u} = -\frac{1}{\rho} \nabla \tilde{p} + \nu \nabla^2 \tilde{u} + \nabla \cdot (\tilde{u}\tilde{u} - \widetilde{u}\widetilde{u}) + \tilde{f}, \quad (9)$$

where \sim denotes a spatial filter—a box filter in the present analysis. The term $\nabla \cdot \tau$ is introduced by spatial filtering of the non-linear term in the Navier–Stokes equation. The balance between $\nabla \tilde{p}$ and $D\tilde{u}/Dt + \nabla \cdot \tau - \nu \nabla^2 \tilde{u}$ in Eq. 9 indicates the impact of $\nabla \cdot \tau$ on the filtered pressure field (\tilde{p}) should be evaluated. The isotropic turbulence DNS velocity field is 3D box-filtered at different filter scales (Δ), ranging from 3 to $15\Delta x$ ($\Delta x = \Delta y = \Delta z$). The acceleration calculated from \tilde{u} , which would be available from under-resolved experimental data, is utilized to reconstruct the pressure field

using Omni3D. The results are compared with the box-filtered pressure (\tilde{p}) field calculated using the original unfiltered data. Figure 7a shows the relative error for the same plane discussed in Fig. 4 for $\Delta/(\Delta x) = 5$. The spatially averaged RMS error for this sample is $(p - p_{DNS})_{RMS}/TKE = 0.03$. To verify this error is associated with the SGS stress, when the pressure field integrated from $D\tilde{u}/Dt + \nabla \cdot \tau$, the scaled error in pressure, shown in Fig. 7b, decreases to 0.4%. Figure 7c indicates that the RMS error increases almost linearly with increasing $\Delta/(\Delta x)$. Considering that $p'_{RMS}/TKE = 0.5$ for the isotropic turbulence field, for a filter size of $\sim 9\Delta x$, the uncertainty in pressure is already in the order of 40% in of p'_{RMS} .

In addition to the spatial resolution of the data, the line spacing used during integration and the number of grid points defining the angles might also affect the accuracy of pressure integration. If they do not maintain the original resolution of the data, they implicitly cause spatial filtering. In contrast, one would expect that the computation speed would decrease as the grid becomes coarser. In this context, inhomogeneity in the grid might also affect the accuracy and efficiency of the Omni3D procedure. Several tests are performed to quantify these effects. In the first series, line spacing is fixed at $1.0\Delta x$, but the number of grid points (i.e., angles) varies from 0.008 times to 3 times the resolution needed for matching the data ($M = 10,242$). Two kind of grids are used, namely a uniform mesh and a graded mesh generated by varying the edge length of the triangles linearly with distance from the North Pole from 0.05 to 2.0 of edge length in the corresponding uniform mesh. The comparison between uniform and graded meshes is aimed at determining whether bias in the number of integration lines introduced by the latter procedure affects the quality of the Omni3D data. All the computations are performed using the original acceleration field calculated from the DNS data. The resulting

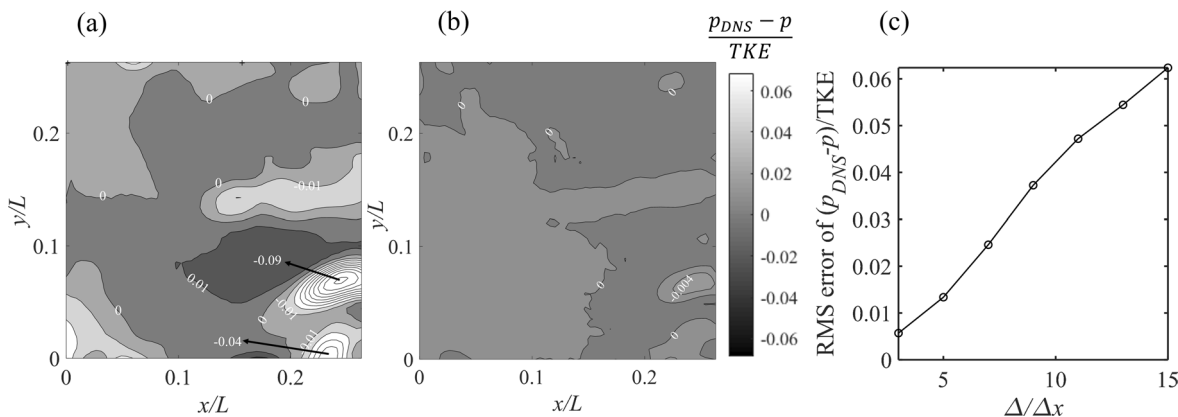


Fig. 7 The SGS stress effects on the pressure calculations for isotropic turbulence: **a** A sample plane showing the error caused by integrating $D\tilde{u}/Dt$ using a $5 \times 5 \times 5$ box-filtered data (increment between

lines -0.01), and **b** the corresponding negligible error caused by integrating $D\tilde{u}/Dt + \nabla \cdot \tau$, and **c** effect of filter size on the spatially averaged RMS error of pressure

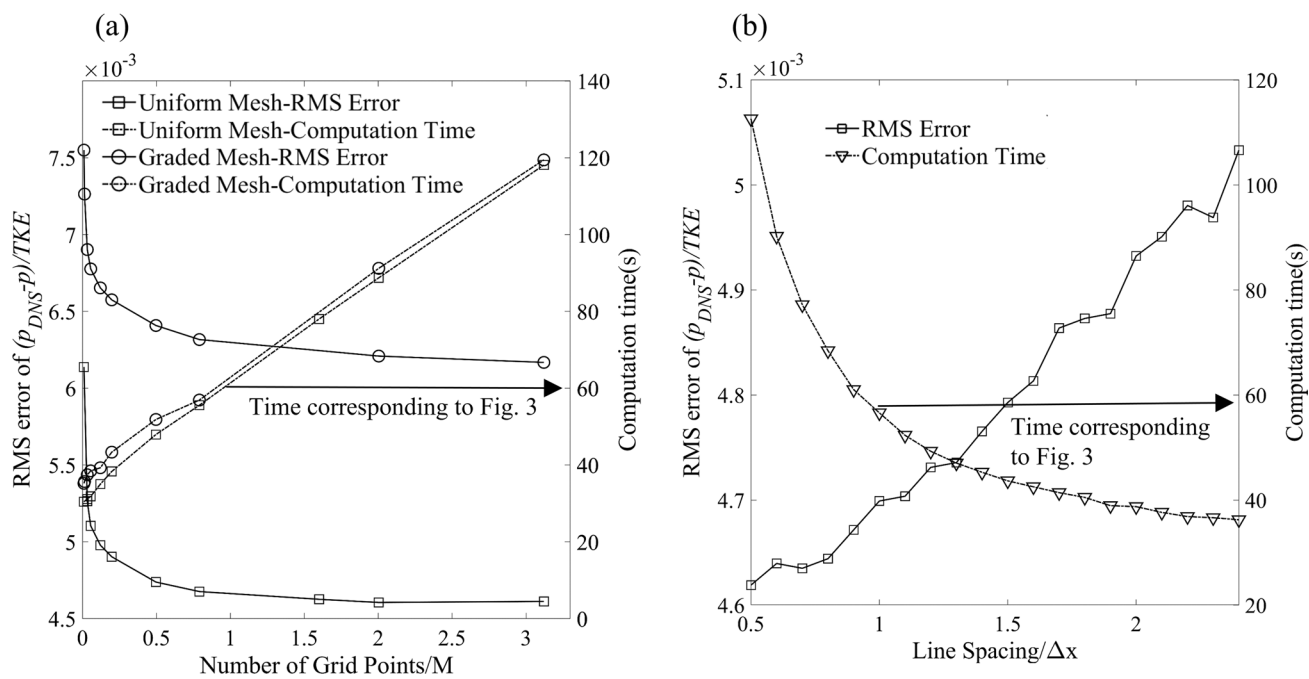


Fig. 8 Effects of: **a** the number of grid points and mesh uniformity, and **b** parallel line spacing on the spatial RMS error in pressure and computation time using Omni3D

pressure error and computation time are plotted in Fig. 8a. As is evident (and expected), the error decreases and the computation time increases with increasing number of grid points. The increase in computation time is linear, at least for the present range, but the decrease in error diminishes when the number of grid point is matched with the data resolution. Hence, there is no advantage in increasing the number of grid points beyond the matching level. Using an inhomogeneous grid increase the error by about 35% for a matched grid. In the second set of tests, the number of grid points is fixed at 10,242, and the line spacing is increased from $0.5\Delta x$ to $2.5\Delta x$. The results shown in Fig. 8b indicate that the computation time grows exponentially and the RMS error decreases linearly with decreasing line spacing. For this range, the impact of varying the line spacing on the error is small, implying that there is limited advantage in increasing the resolution below $1.0\Delta x$. Conversely, increasing the spacing to, e.g., $2\Delta x$, increases the error by 5%, and reduces the computation time by 32%.

3.2 Error analysis for a turbulent channel flow

3.2.1 Uncertainty in velocity and pressure based on synthetic particle traces

Velocity, pressure and particle positions are fetched from the JHU DNS Database for a turbulent channel flow at $Re_\tau = u_\tau h / v = 1000$ (Graham et al. 2016) where u_τ is the

friction velocity and h is half channel height. The concentration of randomly distributed synthetic particles is set to maintain 11 particles per interrogation window, matching the optimum recommended in Atkinson et al. (2011). Hence, it increases with decreasing interrogation volume size. Information about the voxel and interrogation volumes involved for the different cases is provided in Table 1. The particle traces have a 3-D Gaussian intensity distribution, which is converted to discrete values in $5 \times 5 \times 5$ voxel based on the integration model (Lecordier and Westerweel 2004). A thin buffer region is added around the sample volume to allow the particles to enter and leave the simulated measurement domain. The particles are placed at time t , and then translated based on the DNS velocity forward and backward in time by $\pm \Delta t$ and $\pm 2\Delta t$, where Δt varies to maintain maximum particle displacement of less than 12 voxels. The velocity is interpolated using Lagrangian 6th order interpolation to reflect the exact location of the particle center, and its displacement is calculated using the above-mentioned method of Yu et al. (2012). The $5 \times 5 \times 5$ voxel intensity distribution is recalculated once the 3D location of the displaced center is determined. Both cross-correlation-based PIV and Particle Tracking Velocimetry (PTV) are used to calculate the velocity field. Three voxel sizes are used, namely $20/32\delta_v$ (Case I), $10/32\delta_v$ (Case II), and $5/32\delta_v$ (Case III), where $\delta_v = v/u_\tau$. For 3D PIV, the interrogation volume is mostly $32 \times 32 \times 32$ (D_x, D_y, D_z) voxels with 50% overlap except for one case with $32 \times 16 \times 32$ voxels. The corresponding scales in wall

Table 1 Parameters for synthetic PIV analysis

	Case I	Case II	Case III
Particle size	$5 \times 5 \times 5$	$5 \times 5 \times 5$	$5 \times 5 \times 5$
Voxel number	$1000 \times 800 \times 600$ $0.63 h \times 0.5 h \times 0.38 h$	$1000 \times 800 \times 600$ $0.31 h \times 0.25 h \times 0.19 h$	$1000 \times 2000 \times 300$ $0.16 h \times 0.31 h \times 0.05 h$
Voxel size	$0.625\delta_v$	$0.313\delta_v$	$0.156\delta_v$
Interrogation volume	$32 \times 32 \times 32$ voxels	$32 \times 32 \times 32$ voxels	(a) $32 \times 32 \times 32$, 50% overlap (b) $32 \times 16 \times 32$, 50% overlap
$D_x \times D_y \times D_z$	50% overlap	50% overlap	(a) $32 \times 32 \times 32$, 50% overlap (b) $32 \times 16 \times 32$, 50% overlap
$D_x^+ \times D_y^+ \times D_z^+$	$20 \times 20 \times 20$	$10 \times 10 \times 10$	(a) $5 \times 5 \times 5$ (b) $5 \times 2.5 \times 5$
Vector spacing	$10\delta_v \times 10\delta_v \times 10\delta_v$	$5\delta_v \times 5\delta_v \times 5\delta_v$	(c) $2.5\delta_v \times 2.5\delta_v \times 2.5\delta_v$ (d) $2.5\delta_v \times 1.25\delta_v \times 2.5\delta_v$
Particle displacement	Max: 12 voxels = $7.5\delta_v$ Near wall: 0.5 voxels	Max: 12 voxels = $3.75\delta_v$ Near wall: 0.5 voxels	Max: 12 voxels = $1.87\delta_v$ Near wall: 0.5 voxels

units (D_x^+, D_y^+, D_z^+), where $D_x^+ = D_x/\delta_v$, are also provided. Since $u_\tau \sim 0.044U_c$, a free stream displacement of 12 voxels implies that the near-wall displacement is about 0.5 voxels and the near-wall displacement gradient is about 0.35, 0.175, and 0.08 voxels/voxel for case I, II, and III. As discussed later, these values have substantial effect on the accuracy of near-wall acceleration and pressure measurements. The velocity is calculated using multi-pass cross-correlation with window deformation using the commercial LaVision Davis® 8.1 software. Following de Kat and van Oudheusden (2012) and Liu and Katz (2013), the material acceleration at time t is calculated from the five successive 3D particle distributions. The calculated 3D displacements between time $t - \Delta t$ and t ($\Delta x_{-\Delta t}$), and between t and $t + \Delta t$ ($\Delta x_{+\Delta t}$) are used for determining the location of the same particle group in previous ($x + \Delta x_{-\Delta t}$), and subsequent time steps ($x + \Delta x_{+\Delta t}$). Then, the material acceleration is

$$\frac{Du}{Dt}(x, t) \approx \frac{u(x + \Delta x_{+\Delta t}, t + \Delta t) - u(x + \Delta x_{-\Delta t}, t - \Delta t)}{2\Delta t}, \quad (10)$$

where $u(x + \Delta x_{\pm \Delta t}, t \pm \Delta t)$ is determined from by cross correlating the images at times t and $t \pm 2\Delta t$.

For the PTV-based error analysis, it is based on the known position of particles, i.e., it does not include issues related to improper matching of traces between exposures. Only Case III is used for PTV. The velocity of each particle is calculated using a second-order polynomial fit to its centroid ($x_p(t)$), and calculating the time derivative of the fitted displacement. The unstructured results are fitted onto a regular grid using a second-order singular value decomposition (SVD). The principles of SVD are introduced in Golub and Loan (1996), and application of its first-order version for interpolation of holographic PTV data is described in Sheng et al. (2006). The second-order SVD procedures (Talapatra and Katz 2013) express the spatial distribution

of the velocity components based on a second-order 3D Taylor expansion, i.e., using both first- and second-order spatial derivatives. The ellipsoidal interpolation volume is $32 \times 16 \times 32$ voxels, with 3D 50% shift between volumes, and the particle density is increased to make sure that there are enough particles inside each ellipsoid. Using a second-order Taylor series expansion in space for the velocity of each particle, this procedure accounts for the location of this particle relative to the grid point, and the SVD interpolation provides both the velocity and its spatial gradients. The acceleration of each particle is determined from a second derivative of its fitted trajectory, i.e., $Du/Dt(x_p, t) = \ddot{x}_p(t)$. Then SVD interpolation is used for mapping the acceleration onto a regular grid.

Figure 9a–c shows the effect of spatial resolution (cases) on the RMS error in the three velocity components scaled by inner variables ($u^+ = u/u_\tau$), and Fig. 9d–f presents the corresponding RMS errors in acceleration ($a^+ = a\delta_v/u_\tau$). The effects of resolution on errors in velocity have been investigated extensively (Atkinson et al. 2011; de Silva et al. 2011; Worth et al. 2010) and are provided here as a basis for discussion about the acceleration errors. As is evident, and expected, the RMS errors in velocity decrease with increasing resolution, especially in the viscous and buffer layers ($y^+ < 30$). The highest errors are associated with the streamwise components. The present trends and values are consistent with the synthetic data-based analyses for 2D boundary layers reported by Atkinson et al. (2011), where $D_x = D_y = 12.5$, and the LaVision results for Case B of PIV Challenge No. 2 (Stanislas et al. 2005), where $D_x^+ = D_y^+ = 3.12$. For all components, there is a striking decrease in error when $D_x = D_y$ is decreased to 5.0, and a further decrease when D_y^+ is reduced to 2.5. The improvement is associated with a reduction in the extent of velocity change across the interrogation window, which for boundary layers occurs predominantly in the wall-normal

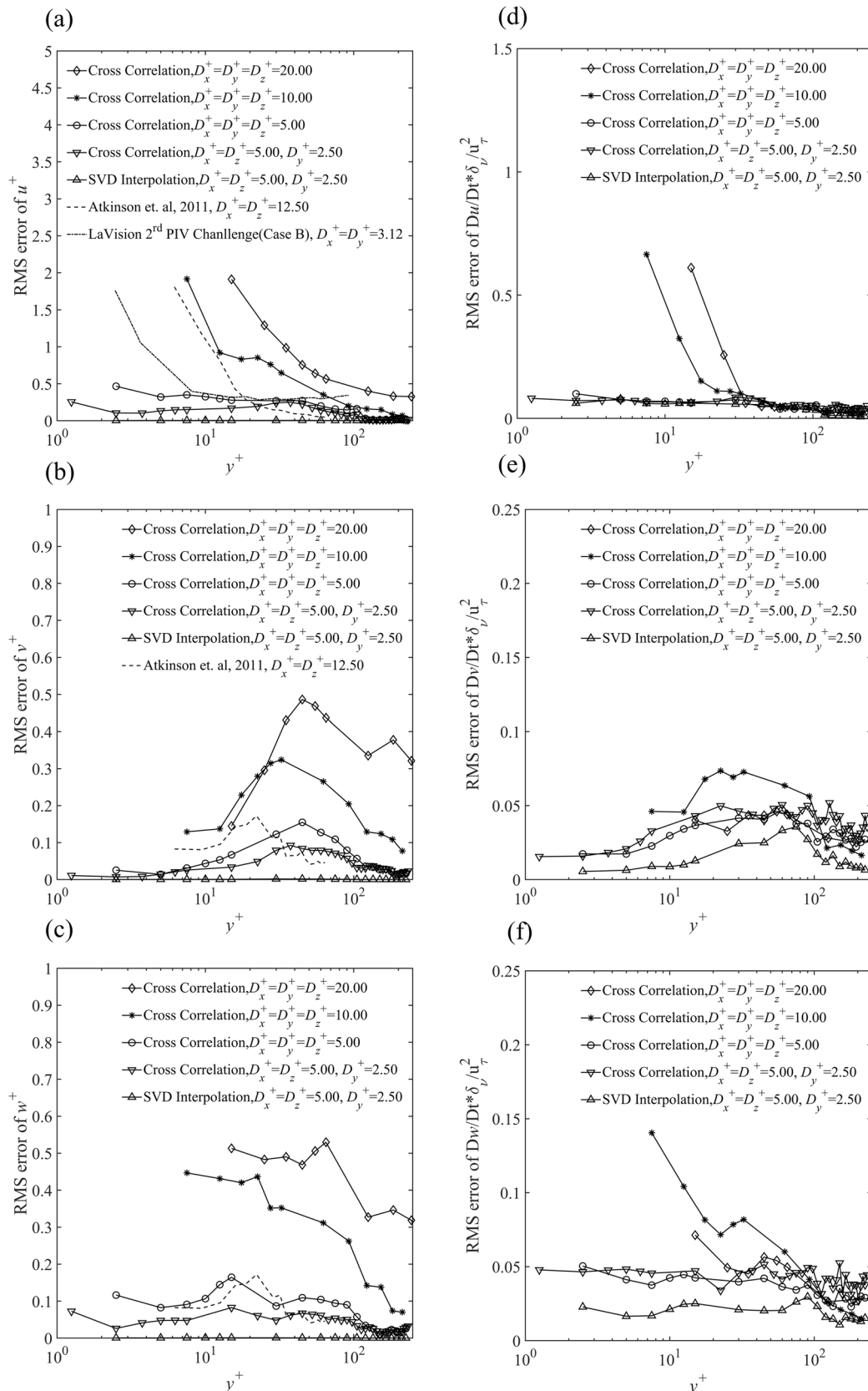


Fig. 9 Effects of data resolution and velocity calculation method on the accuracy of **a** u , **b** v , **c** w , **d** Du/Dt , **e** Dv/Dt , and **f** Dw/Dt for the synthetic channel flow data generated from the JHU database

direction. In the present analysis, as D_y^+ is reduced from 10 to 5 and to 2.5, the displacement difference across the window decreases to 5.6, 2.8, and 1.4 voxels, respectively. The PTV–SVD results have by far the lowest errors. As discussed in Talapatra and Katz (2013) for experimental holographic microscopy data, the improvements are caused by accounting for the exact location of each particle in space during interpolation onto a regular grid. The errors in acceleration include effects of shifting of the interrogation window and velocity calculations. Similar to the trends of the velocity, the highest acceleration errors are associated with the streamwise component, for which $\epsilon_{Du/Dt} \sim \epsilon_u u_\tau / \delta_v$, and they decrease with increasing resolution, especially when the $D_x^+ = D_y^+ = D_z^+$ are reduced to 5.0. However, unlike the velocity, further reduction in D_y^+ to 2.5 has a minimal effect. Yet, using PTV–SVD at the same resolution achieves further improvements.

Figure 10a focuses on the effect of spatial resolution on the spatial RMS error of the dimensionless pressure ($p'^+ = p' / \rho u_\tau^2$) over the sample volume calculated using Omni3D. Consequently, the integration includes the viscous terms, i.e., $\nu \nabla^2 \mathbf{u} - \mathbf{D}\mathbf{u}/Dt$. As a reference, the plot also includes the profile of the temporal RMS value of pressure fluctuations, p'_{RMS}^+ available from the DNS data (Graham et al. 2016). In all the plots, the scales for p'_{RMS}^+ are located on the right vertical axis. As is evident, the error in pressure decreases substantially as $D_x^+ = D_y^+ = D_z^+$ is reduced to 5. Similar to the trends of the acceleration, the impact of

further decrease in D_y^+ to 2.5 does not influence the results, but application of PTV–SVD causes a significant reduction in error, to less than 2% of p'_{RMS}^+ across the entire boundary layer. The results obtained for the two coarsest interrogation windows are high, reaching 40% of p'_{RMS}^+ in the viscous and buffer layers, but decreasing to 20% and 8% for $D_y^+ = 20$ and 10, respectively, in the log layer. Keeping the interrogation window at $D_x^+ = 5$, maintains an error of ~6% over the entire channel. Note that the error spike at $y^+ = 80$ for $D_x^+ = D_y^+ = D_z^+ = 10$ is associated with the specific instantaneous data used in the present study, and is not a feature of the calculation procedures. As a demonstration, Fig. 10b compares the RMS error for different samples showing that the instantaneous profiles fluctuate and the spike disappears once several realizations are averaged (the diamond represents the data currently used).

Next, the performance of the previously introduced four methods for integrating the pressure is compared for two interrogation window sizes. The discussion starts with the PTV–SVD-based results, where the acceleration errors are very low. The viscous terms are included in all cases. As is evident from Fig. 11a, b, the Omni3D and PPE-Omni2D methods give essentially identical results for $D_y^+ = 5$, consistent with the results for isotropic turbulence (Fig. 11a). However, for $D_y^+ = 2.5$ (Fig. 11b), the Omni3D errors are significantly lower than those of PPE-Omni2D both in the viscous and buffer sublayers as well as near the Dirichlet boundary. In the outer layer, the better performance is (most

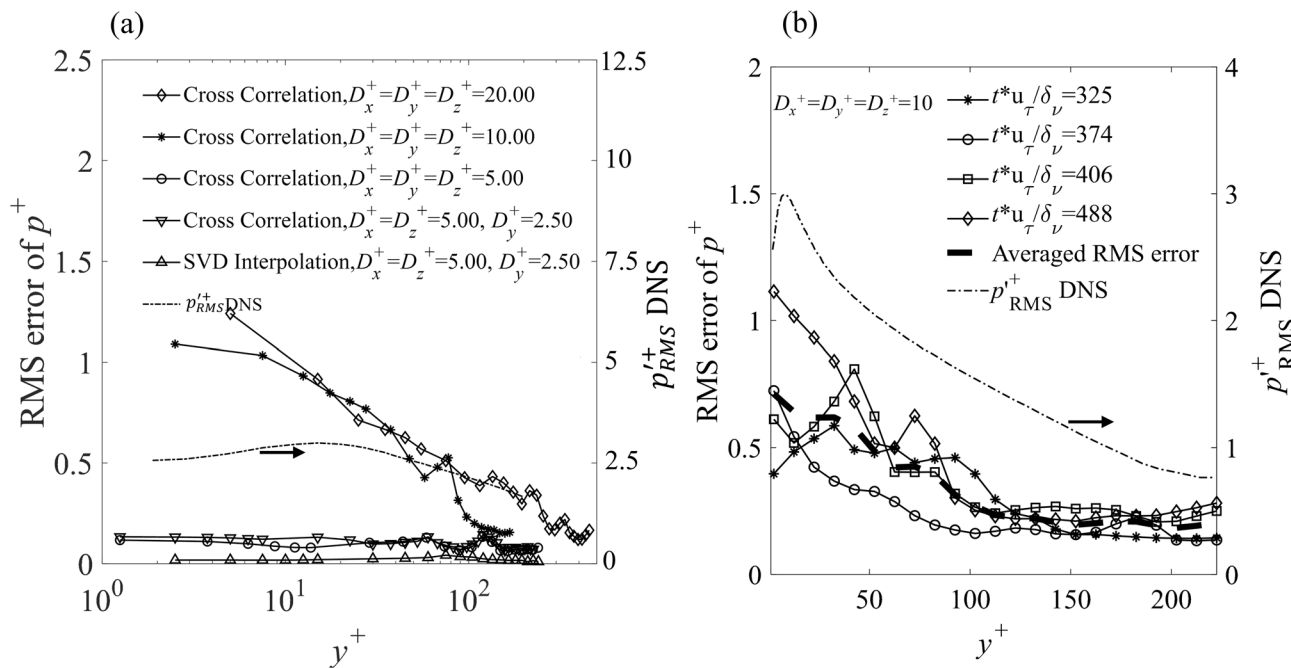


Fig. 10 **a** Effects of data resolution and method for calculating the velocity on the spatial RMS error in channel flow pressure. **b** Variations of spatial RMS error in channel flow pressure for different

samples. For all the samples, $D_x^+ = D_y^+ = D_z^+ = 10$. Dashed dotted line: DNS temporal RMS pressure fluctuations, with scales located at the right axis, as indicated by the arrow

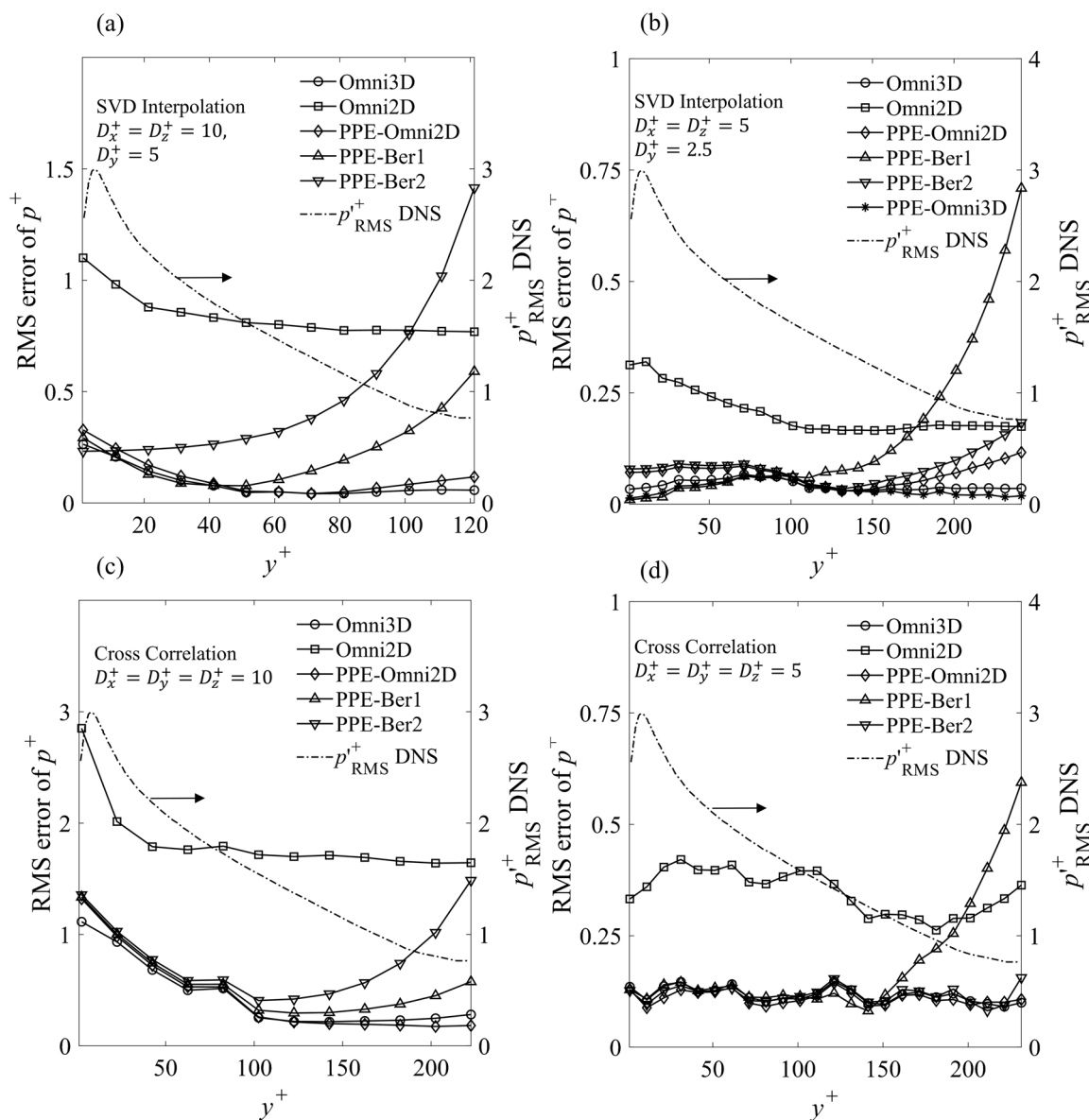


Fig. 11 Effects of data resolution, method for calculating the velocity, and integration procedure on the spatial RMS error in channel flow pressure: **a** PTV-SVD data with $D_x^+ = D_z^+ = 10, D_y^+ = 5$; **b** PTV-SVD data with $D_x^+ = D_z^+ = 5, D_y^+ = 2.5$; **c** cross correlation 3D PIV with $D_x^+ = D_y^+ = D_z^+ = 10$, and **d** cross correlation 3D PIV with $D_x^+ = D_y^+ = D_z^+ = 5$. Dashed dotted line: DNS temporal RMS pressure fluctuations, with scales located at the right axis, as indicated by the arrow

likely) associated with better matching of the boundary values with those in the inner part of the flow field. To verify this statement, we have repeated the integration using the Omni3D results as a Dirichlet BC for the PPE method (i.e., PPE-Omni3D). In this case, the error decreases to levels that are very close to those of the Omni3D results for the outer layers. The same applies to the (minor) increase in error of PPE-Omni2D in the inner layer, i.e., this error also diminishes if Omni3D data are used for the Dirichlet BC in the outer layer. The PPE-Ber1 and PPE-Ber2 results are erroneous in the vicinity of the Dirichlet boundary, as expected,

but this error diminishes with increasing distance from this surface, matching the PPE-Omni2D near the opposite surface. The decreasing impact of the Bernoulli BC with distance has already been noted by Ghaemi et al. (2012). They observe that the effect on the wall pressure diminishes when the Dirichlet BC is imposed at $y/\delta > 0.2$. This conclusion is consistent with the present findings both for the channel flow as well as for isotropic turbulence. The Omni2D errors are 32% of p'^+_{RMS} over the entire flow domain for the coarse data, decreasing to less than 10% with increasing resolution. For the PIV-based analysis, the results for the

coarse and higher resolution data are presented in Fig. 11c, d, respectively. As expected, in all cases, the errors are much higher than those based on the PTV data. The Omni3D and PPE-Omni2D errors follow very similar trends for both the coarse and finer data, with the significant increase near the wall, and a reduction to $\sim 8\%$ in the outer layer. For the higher resolution data, the error remains at about 5% over the entire domain. The PPE-Ber1 and PPE-Ber2 results increase near the Dirichlet interestingly to the same level as the PTV results, indicating that improvements in the data quality do not compensate for the errors introduced by the boundary conditions. Finally, the Omni2D errors are high across the entire boundary layer, reaching 60% of p_{RMS}^+ in the outer boundary and 100% near the wall for the coarse data. Increasing the resolution decreases this error uniformly to $\sim 10\%$.

The effect of the viscous term is summarized in Fig. 12a, b for the fine, $D_x^+ = D_y^+ = D_z^+ = 5$, and corresponding PTV-SVD data in Fig. 12b. As is evident, not including the viscous term in the buffer and viscous sublayers increases the error in the near wall region by about three times for the PIV data and by about five times for the PTV-SVD data. Hence, the improved data quality is overwhelmed by the missing viscous terms. The differences diminish in the log region. These trends are consistent with the findings of Ghaemi et al. (2012).

3.2.2 Improvements by avoiding high-error zones

As discussed in Sect. 3.1.2, the error propagation by the Omni3D method is predictable when the acceleration error distribution is known. This section explores whether the error in pressure can be reduced if the contribution of integration paths carrying large errors is suppressed. The acceleration error can be quantified from the curl of acceleration in situations where the exact values are not known. (Lynch and Scarano 2014) or $\zeta = \nabla \times (-D\mathbf{u}/Dt + \nu \nabla^2 \mathbf{u})$ if the viscous term is included. For convenience, ζ is still referred to as acceleration error in the following analysis. Two ways to remove or weaken the effect of paths carrying large errors are proposed here. In the first, the “selected path” method (Omni3D-SP), certain path-carrying errors exceeding a prescribed level are avoided. This threshold level is determined, e.g., from the spatial histogram of $|\zeta|$. During integration using PLODI, the local magnitudes of ζ are compared to the selected threshold. Once a high-error point is identified, this path is not used during the boundary pressure iteration phases (steps 2 and 3, Fig. 2). Subsequently, for internal pressure calculation (step 4), the integration along this path stops at the error point, and then restarted in the following point, preventing the propagation of this error to the low-error zones. Once an integration path is stopped and restarted further along, the new values do not contain direct information originating from the terminated line. Instead, the algorithm utilizes the pressure at the starting point,

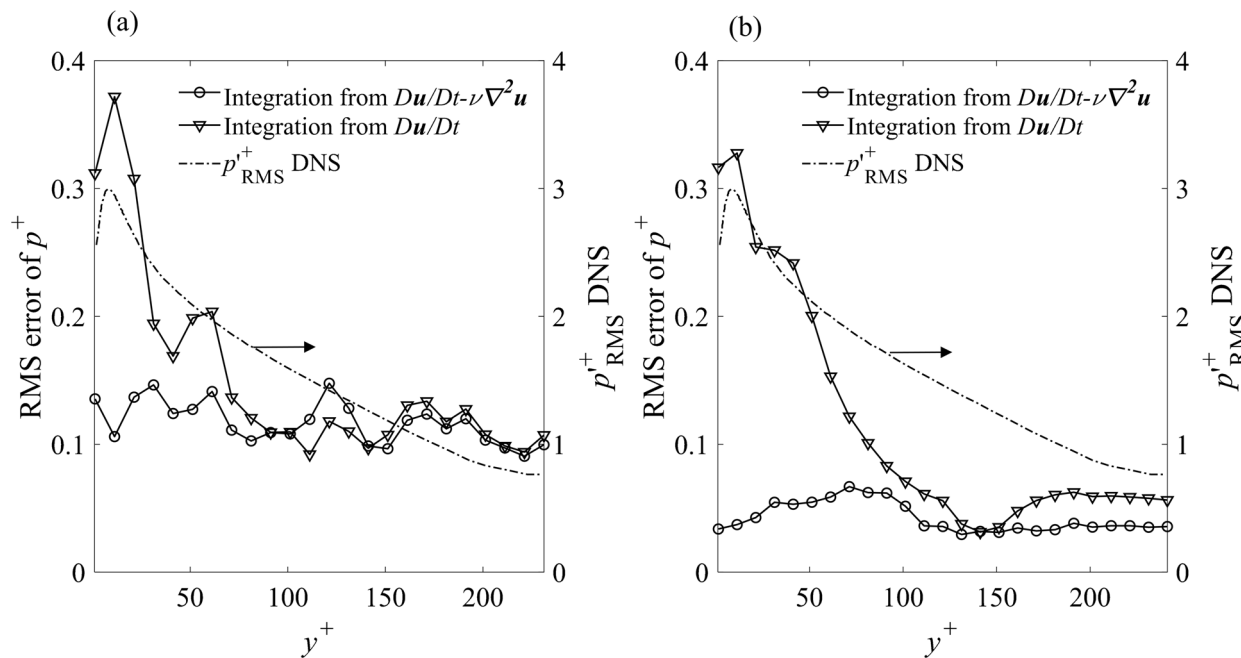


Fig. 12 Effect of viscous stress on the spatial RMS error of channel flow pressure for **a** cross correlation with $D_x^+ = D_y^+ = D_z^+ = 5$, and **b** PTV-SVD with $D_x^+ = D_z^+ = 5$, $D_y^+ = 2.5$. Dashed dotted line: DNS

temporal RMS pressure fluctuations, with scales located at the right axis, as indicated by the arrow

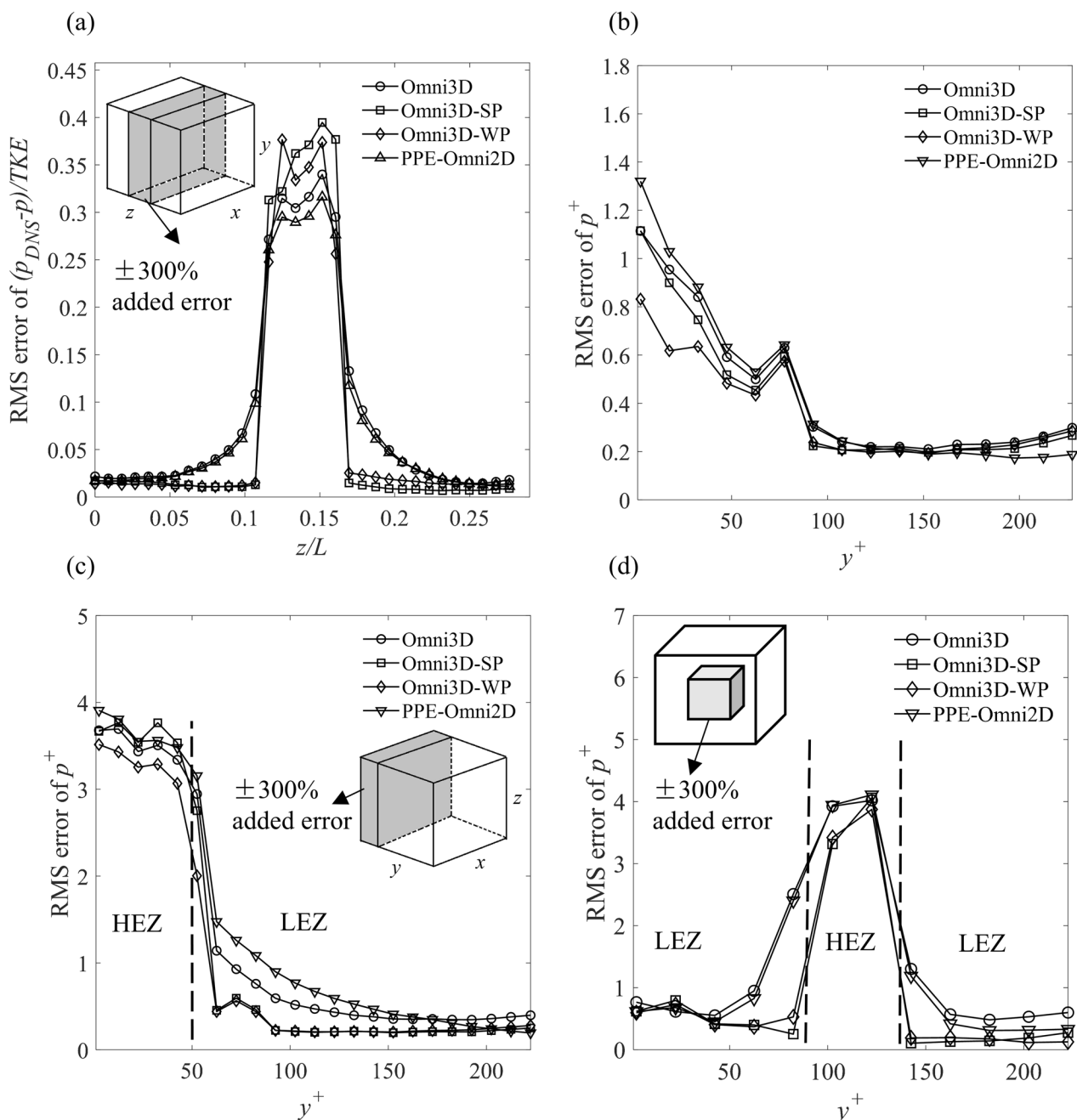


Fig. 13 Effect of implementing the selected paths (Omni3D-SP) and weighted paths (Omni3D-WP) methods, both based on the magnitude of $\nabla \times \frac{Du}{Dy}$, on the spatial RMS error in pressure for: **a** isotropic turbulence with $\pm 300\%$ acceleration error embedded at $0.12 < z/L < 0.16$,

b synthetic channel flow data with $D_x^+ = D_y^+ = D_z^+ = 10$, **c** data in **b** with $\pm 300\%$ acceleration error embedded at $y^+ < 50$, **d** data in **b** with $\pm 300\%$ acceleration error embedded in the central cube with side of $50\delta_v$

which is calculated by integration from all directions (without stopping) except for the stopped ones. Hence, effects of pressure gradients in the region with bad data are accounted for. In the second, the “weighted path” method (Omni3D-WP), each integration path is given a weight, which is inversely proportional to the average value of $|\zeta|$ along this

path. The integration is then performed following the regular procedures in all phases, but using the weighted values.

Several tests have been used to evaluate the impact of this method. First, Fig. 13a presents the results for the isotropic turbulence data with the strip containing embedded 300% error in acceleration discussed in Sect. 3.1.2 (Fig. 6a). As is evident, both techniques reduce the RMS error in pressure

for regions located outside of the high-error zone. The test utilizes the $D_x^+ = D_y^+ = D_z^+ = 10$ channel flow data that has considerable error near the wall (Figs. 9e, 11c). The histogram-based threshold level is set by specifying that 25% of the data are erroneous, which in this case is concentrated mostly near the wall. The result presented in Fig. 13b shows that Omni3D-WP reduces the error near the wall by as much as 35% in comparison to the original Omni3D data, reducing the uncertainty to 32% of p_{RMS}' . The improvements with diminishing levels extend to $y^+ = 120$. Omni3D-SP shows limited effect near the wall, but matches the other method close at $y^+ > 50$. Interestingly, near the outer boundary, the PPE-Omni2D achieves errors lower than the other techniques. This trend occurs since the Dirichlet boundary condition used for PPE-Omni2D is not affected by the high-error zones near the wall, while all the Omni3D procedures involve 3D integration to determine the boundary conditions. Hence, they are influenced by the near-wall errors. The jump in error at $y^+ = 70$ is associated with the specific DNS data used in the present analysis as shown in Fig. 11b, where the edge of the buffer layer contains a series of small eddies. It disappears when the resolution is increased (Fig. 10) or if the same procedures are used to analyze another set of instantaneous data from the DNS channel flow database. Next, a 300% acceleration error is randomly added to the near-wall region ($y^+ < 50$) of the $D_x^+ = D_y^+ = D_z^+ = 10$ results. The resulting RMS error pressure profiles in Fig. 13b show that within the high-error region, the weighted path method has the best performance. At $y^+ > 50$, both Omni3D-WP, and Omni3D-SP achieve similar significant reduction in error propagation into the log layer, reducing the RMS error in pressure by 60% compared to Omni3D and by 80% compared to PPE-Omni2D. Finally, the effect of bad spots in the channel flow acceleration is examined by adding a 300% randomly distributed noise to a cube with side of $50\delta_\nu$, centered at $y^+ = 115$. The RMS errors in pressure averaged over the entire depth are presented in Fig. 13d. Clearly both Omni3D-WP and Omni3D-SP reduce the error within the high-error zone, and rapidly suppresses its propagation into regions located outside of it.

4 Experimental applications

4.1 Experimental setup

The experimental data have been obtained as part of a study to characterize a turbulent channel flow over a compliant surface and involve simultaneous measurements of the 3D flow structure using TPIV and the wall deformation using Mach-Zehnder Interferometry. The measurement procedures are described in Zhang et al. (2015), and detailed data on flow-deformation interactions are provided in Zhang et al.

(2017). These interactions are investigated by calculating the pressure distribution using Omni3D, and correlating it with the wall dynamics. The procedures associated with Omni3D are only mentioned briefly in that paper, and the present paper is the first introducing and evaluating it in detail. The experiments have been performed in the acrylic 3.3 m long, 50.8×203.2 mm channel flow extension to the refractive index-matched facility at Johns Hopkins University. The compliant wall made of polydimethylsiloxane (PDMS) starts 1900 mm away from the beginning of the channel (74.8 half channel height, $h = 25.4$ mm), i.e., when the flow is fully developed, and has dimensions of $1250 \times 16 \times 203.2$, in the x , y , and z directions, respectively. The working fluid is a 62% by weight aqueous solution of sodium iodide with $\rho = 1.8 \times 10^3$ kg m $^{-3}$, and $\nu = 1.1 \times 10^{-6}$ m 2 /s. The free stream velocity is 2.5 m/s, the friction velocity is 0.102 m/s, and $Re_\tau = 2300$. The velocity is measured using TPIV. The sample volume is $30 \times 10 \times 10$ mm 3 . The 1200×600 pixels images are recorded by four pco.dimax high-speed cameras at 6 kHz, and LaVision® software is used for calibrating and reconstructing the particle field, as well as for calculating the velocity by multi-pass volumetric cross-correlations. With a volume of $1380 \times 638 \times 611$ voxels, voxel size of 18.8 μm , the interrogation volume is $48 \times 48 \times 48$ voxels with 75% overlap between volumes. The resulting velocity field consists of $100 \times 47 \times 38$ vectors, with spacing of 0.226 mm. In wall units, the interrogation window size is 80, i.e., the data are coarse based on the criteria and analysis presented in the previous sections. The results are used for calculating the material acceleration and pressure, using procedures described in Sect. 3.2.1. Further details about the experimental procedures can be found in Zhang et al. (2017). It should be noted, that for these measurements, the compliant wall is quite stiff, and the deformation amplitude is well below 10% of the wall unit.

4.2 Comparisons of pressure snapshot, statistics, and correlations

Sample instantaneous realizations of pressure field calculated by Omni3D-WP, Omni2D, PPE-Omni2D, and PPE-Ber1 superimposed on the velocity vectors (diluted by 2) are plotted in Fig. 14a–d, respectively. As done for the synthetic data, in all cases, the spatially averaged pressure is set to zero. In general, as expected, the pressure minima are typically associated with vortical structures, and the near-wall maximum is located at the transition from a sweeping to an ejection event, consistent with findings by Kim and Adrian (1999), Ghaemi and Scarano (2013), and Joshi et al. (2014). The near-wall pressure peak of the Omni2D results are substantially higher than those of the others, but the other three appear to be qualitatively similar. Corresponding profiles of the RMS values of pressure fluctuations are presented

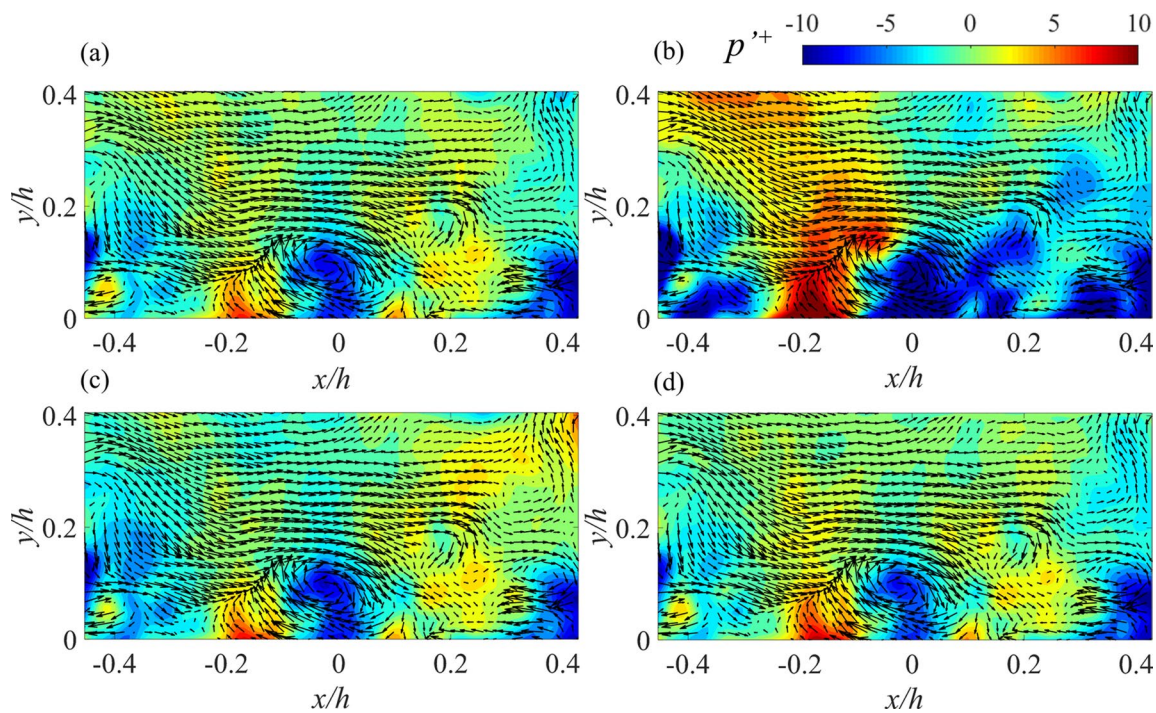


Fig. 14 Pressure calculated from under-resolved experimental data. ($D_x^+=D_y^+=D_z^+=80$) Computed instantaneous pressure field combined with velocity vectors calculated using: **a** Omni3D-WP, **b** Omni2D, **c** PPE-Omni2D, and **d** PPE-Ber1

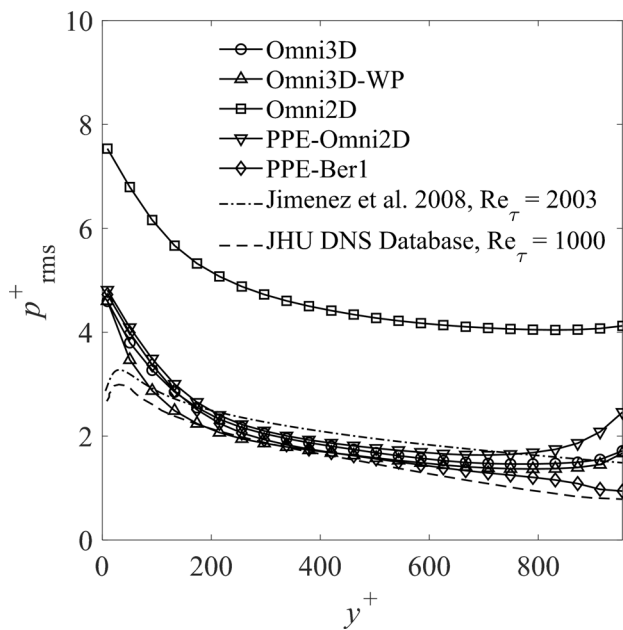


Fig. 15 Profiles of the experimental ($D_x^+=D_y^+=D_z^+=80$) temporal RMS pressure fluctuations calculated using several integration methods in comparison to available DNS data

in Fig. 15 along with published DNS data retrieved from two databases, including the previously mentioned JHU data for $Re_\tau=1000$ (Graham et al. 2016), and the data provided

by Jimenez and Hoyas for $Re_\tau=2003$ (Jimenez and Hoyas 2008). As is evident, the Omni2D profile deviates significantly from the rest of the experimental and numerical results. For a significant fraction of the sample area, the Omni3D, Omni3D-WP, PPE-Omni2D, and PPE-Ber1 fall between the DNS-based profiles. In the outer region, the PPE-Omni2D results curve upward and those of the PPE-Ber1 have the lowest values, presumably because of the corresponding conditions along the Dirichlet boundary. In the inner part, $y^+ < 100$, all the experimental results turn upward well beyond the DNS data, consistent with the large errors expected for the present coarse resolution. However, the Omni3D-WP profile is lower than others at $y^+ < 250$, and remains within the DNS domain down to $y^+=80$. This trend adds confidence to the validity of the Omni3D-WP results all the way to the end of the buffer layer.

Spatial streamwise spectra calculated using FFT without any windowing or detrending from the instantaneous pressure distributions along streamwise lines are presented in Fig. 16. They are compared to spatial spectra calculated directly from the JHU DNS pressure field calculated in the same way, as well as to experimental temporal pressure spectra measured using a transducer by Tsuji et al. (2007) for nearly the same Re_τ as the present study. All the spatial spectra are averaged over the spanwise direction as well as over time, hence each curve represents an average of 266,000 lines for the experimental data, and

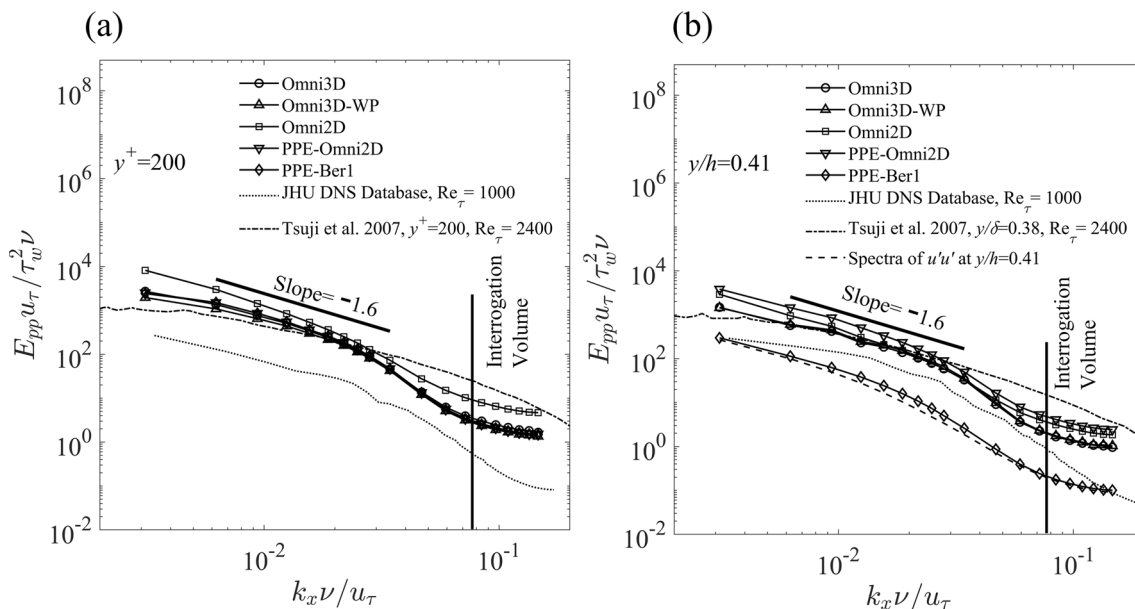


Fig. 16 Ensemble and spanwise-averaged streamwise pressure spectra calculated from experimental data using several methods in comparison to the experimental wall data of Tsuji et al. (2007), DNS data of

Kim and Adrian (1999) and the JHU DNS data (Graham et al. 2016). Elevations are: **a** $y^+=200$, and **b** $y/h=0.41$, at the top surface

60,000 lines for the DNS results. The vertical lines show the wavenumber corresponding to the TPIV window size ($80\delta_v$). Results are provided for two elevations. At $y^+=200$ (Fig. 16a), all the experimental spectra except for the Omni2D results, collapse and fall close to those of Tsuji et al. (2007) up to a wavenumber of ~40% of that corresponding to the interrogation volume size. They also have a range of wavenumbers with the expected slope of -1.6 . The JHU DNS spectrum seems to follow a similar shape, but all the values are lower, presumably because of the differences in Reynolds number. At the upper boundary ($y/h=0.41$, Fig. 16b), the PPE-Ber1 results are substantially lower than the rest, and as prescribed (Eq. 7), are quite similar to the $u'u'$ spectrum. Furthermore, as prescribed, the Omni2D and the PPE-Omni2D nearly collapse. The Omni3D and Omni3D-WP spectra overlap and have the closest agreement with the Tsuji et al. (2007) data up to ~30% of the interrogation volume size wavenumber. Hence, the pressure obtained from the experimental data could be used for calculating pressure spectra provided effects of low-pass filtering by the interrogation window are accounted for. Finally, it would be of interest to compare the pressure–vertical velocity spatial correlations, $r_{d,p}(\Delta x, \Delta y) = \langle p'(x, y = 0.05h, z)v'(x + \Delta x, y + \Delta y, z) \rangle / p'_{\text{RMS}} v'_{\text{RMS}}$, where $\langle \rangle$ indicates ensemble averaging. The vertical velocity component is selected since multiple previous studies have shown that it has the highest correlation with the pressure (Panton et al. 1980; Kobashi and Ichijo

1986; Joshi et al. 2014; Naka et al. 2015). The comparisons presented in Fig. 17 demonstrate that all the pressure integration techniques included (Omni3D-WP, Omni3D, PPE-Omni2D, and PPE-Ber1) reproduce spatial correlation maps with similar shapes, which are consistent with the above-mentioned published data (e.g., Panton et al. 1980). However, the magnitude of the correlation peak obtained using Omni3D-WP is higher than the others. Although it's not shown here, when the pressure at $y/h = 0.18$ is used for the correlations, the corresponding positive correlation peak increases to 0.16, consistent with the value obtained by Joshi et al. (2014) at the same elevation.

5 Conclusions and discussions

An efficient three dimensional, parallel-line, omni-directional integration method (Omni3D) is introduced for calculating the pressure distribution from an experimental 3D velocity field. The number of integration directions and distance between parallel lines are matched with the data resolution since further increase in resolution does not improve the data quality. This method is compared to several approaches, including the previously used Omni2D—the 2D virtual-boundary Omni-directional integration method, and several techniques based on solving the Pressure-Poisson Equation with different Dirichlet boundary conditions. These comparisons are based on

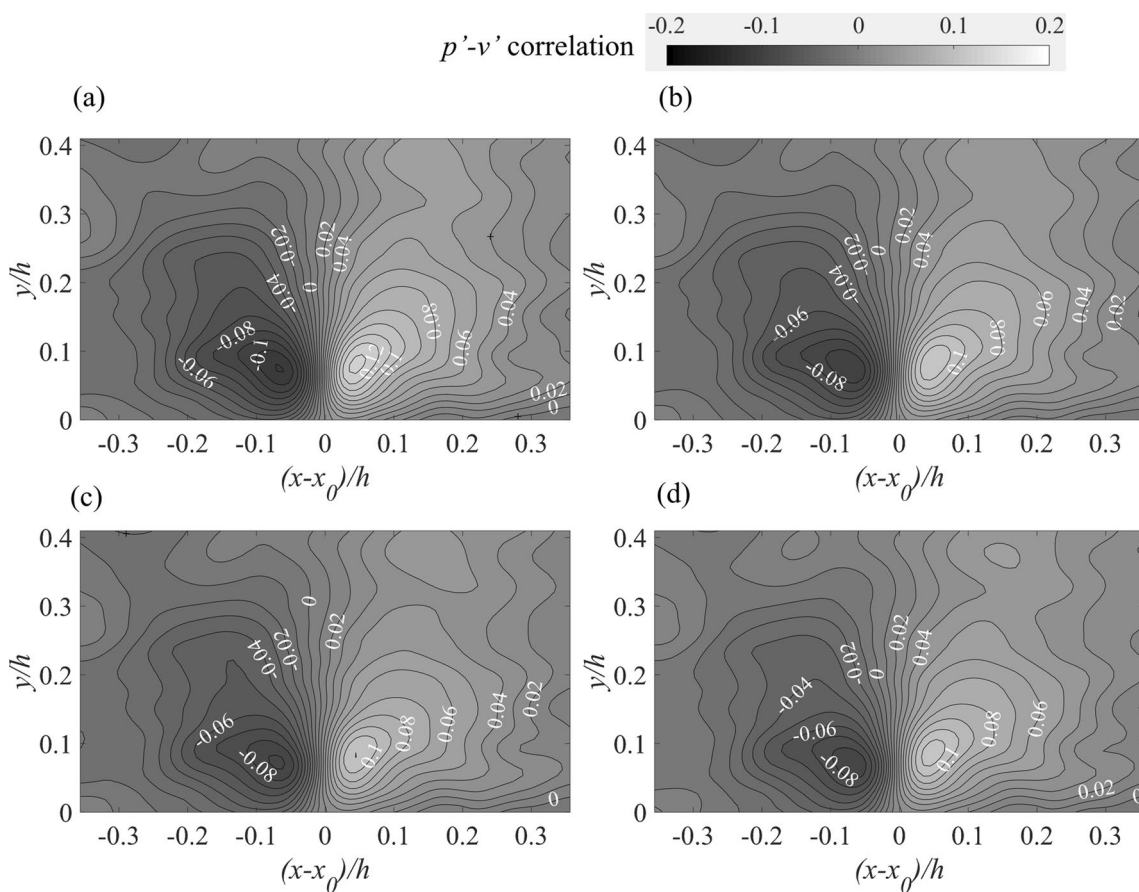


Fig. 17 Spatial correlation of wall-normal velocity fluctuation and near-wall pressure ($y/h=0.05$) calculated using: **a** Omni3D-WP, **b** Omni3D, **c** PPE-Omni2D, and **d** PPE-Ber1. Incremental increase between lines: 0.01

using both DNS data for isotropic turbulence and turbulent channel flow as well as experimental data for a turbulent channel flow. For the DNS channel flow, the analysis is based on generating synthetic particle fields with varying concentrations, and analyzing the velocity fields following established PIV procedures along with particle tracking augmented by application of singular value decomposition to map the data onto regular grids. Subsequently, the Omni3D method is enhanced by adopting selected and weighted-path methods aimed at minimizing the propagation of errors originating from regions where the experimental data have large errors. As implemented, Omni3D offers several advantages: first, there is no need to specify a Dirichlet boundary condition, as commonly done for PPE-based techniques. Instead, an iterative process matches the pressure distribution along the boundary with the internal pressure gradient field. The self-consistent pressure field only misses a constant value. In the present paper, the spatially averaged pressure is set arbitrarily to zero. However, this constant could be provided by, e.g., a point pressure transducer. Another option to avoid prescribing the

Dirichlet pressure distribution in PPE-based calculations is to use Omni2D to generate the pressure distribution along this boundary. In flow with low errors in acceleration Omni3D and PPE-Omni2D give the same pressure distributions. In contrast, using other techniques based on, e.g., Bernoulli's eqn. generate large errors near the Dirichlet boundary. These errors decay with increasing distance from the boundary. Applying Omni2D to make the pressure distribution in the Dirichlet boundary self-consistent reduces the errors originating from this boundary. Yet, Omni3D still performs better, especially when the weighted-path method is applied to reduce the impact of acceleration errors. Presumably, one could develop a weighted-paths method for the PPE solver as well. Such development is beyond the scope of the present study.

Second, Omni3D involved homogeneous integration from all possible directions from the boundary to internal points, preventing any bias in direction, and minimizing the impact of random errors on the pressure distribution. Paths with particularly large errors in pressure gradients, evaluated from the magnitudes of their curl can be readily

avoided. The present tests demonstrate that the weighted path Omni3D method is effective in preventing the propagation of errors. Hence, it is strongly recommended to use the weighted path method instead of using the simple Omni3D. Third, Omni3D can be readily adopted for complex boundaries, including compound ones by terminating the integration along any path and at any point, and restarting it on the opposing boundary, the so-called selected path method. Fourth, while Omni3D involves massive computations, the procedures can be readily parallelized. Using a GPU-based code, the pressure computation is accelerated by more than two orders of magnitudes, enabling efficient processing of large databases. Using an advanced GPU board and the newer Cuda 8.0 toolkit, the computation time of Omni3D is reduced to 10 s for a single realization. In contrast, using the computer CPU for solving PPE-Ber and PPE-Omni2D take about 22 and 27 s, respectively. Hence, while an Omni3D solution is much more computationally intensive than PPE, the highly parallelized GPU-based algorithm brings the computation time to the same order of magnitude. It is possible that a method for weighting paths based on acceleration errors could be developed for PPE-based procedures as well. Such development is beyond the scope of the present study.

The error analysis using synthetic data demonstrate the sensitivity of all the methods for calculating the pressure to the wall-normal resolution of the velocity distribution in the inner part of the boundary layer. It appears that the error decreases substantially as the wall-normal resolution is reduced to about five wall units, a challenge for high Reynolds number flows. Furthermore, the impact of the viscous terms in the inner part of boundary layers is not negligible, and so is the effect of sub-grid stresses, which increases with decreasing resolution. Significant improvements are achieved using particle tracking-based data, and projecting it onto the regular grid using SVD, which accounts for the exact position of each particle relative to the grid point. In this context, as discussed, the present Omni3D implementation is based on an Eulerian Cartesian coordinate system, and involves integration steps along grid points, which have minimal distance from the prescribed parallel line. As noted before, with recent development of 4D-PTV methods, such as the Shake-The-Box (Schanz et al. 2016), a Voronoi-based integration method (Neeteson and Rival 2015) can be used for determining the pressure by applying PPE on the unstructured data (van Gent et al. 2017). Although not done in this paper, Omni3D can be readily implemented in an unstructured system by integration from particle to particle subject to a prescribed constraint on the distance from the integration path. This approach will be implemented and evaluated in future efforts.

Acknowledgements This research has been sponsored by the Office of Naval Research under Grant no. N00014-16-1-2300. The program officer is Debbie Nalchajian.

References

- Atkinson C, Coudert S, Foucaut JM et al (2011) The accuracy of tomographic particle image velocimetry for measurements of a turbulent boundary layer. *Exp Fluids* 50:1031–1056
- Batchelor GK (1951) Pressure fluctuations in isotropic turbulence. *Proc Cambridge Phil Soc* 47(2):359–374
- Baur T, Königter J (1999) PIV with high temporal resolution for the determination of local pressure reductions from coherent turbulent phenomena. In: 3rd international workshop on particle image velocimetry. Santa Barbara, CA, 16–18 September 1999
- Blake W (2017) Mechanics of flow-induced sound and vibration. Academic Press, Cambridge
- Bukov AP, Orlov AA, Mosharov VE, Radchenko VN, Pesetsky VA, Sorokin AV, Phonov SD, Alaty L, Colucci V (1992) Application of luminescent quenching for pressure field measurements on the model surface in a wind tunnel. In: Wind tunnels and wind tunnel test techniques; proceedings of the conference, Southampton, United Kingdom, 14–17 September 1992
- Bull MK (1996) Wall-pressure fluctuations beneath turbulent boundary layers: some reflections on forty years of research. *J Sound Vib* 190(3):299–315
- Charonko JJ, King CV, Smith BL, VLachos PP (2010) Assessment of pressure field calculations from particle image velocimetry measurements. *Meas Sci Technol* 21:105401
- Corcos GM (1963) Resolution of pressure in turbulence. *J Acoustic Soc Am* 35:192–199
- de Kat R, van Oudheusden BW (2012) Instantaneous planar pressure determination from PIV in turbulent flow. *Exp Fluids* 52:1089–1106
- de Silva M, Baidya R, Khashehchi M, Marusic I (2011) Assessment of tomographic PIV in wall-bounded turbulence using direct numerical simulation data. *Exp Fluids* 52:425–440
- Elsinga GE, Scarano F, Wieneke B, van Oudheusden BW (2005) Tomographic particle image velocimetry. In: 6th international symposium on particle image velocimetry. Pasadena, California, USA, 21–23 September 2005
- Ghaemi S, Scarano F (2013) Turbulent structure of high-amplitude pressure peaks within the turbulent boundary layer. *J Fluid Mech* 735:381–426
- Ghaemi S, Ragni D, Scarano F (2012) PIV-based pressure fluctuations in the turbulent boundary layer. *Exp Fluids* 53(6):1823–1840
- Golub GH, Loan CFV (1996) Matrix computation. JHU Press, Baltimore
- Graham J, Kanov K, Yang XIA, Lee MK, Malaya N, Lalescu CC, Burns R, Eyink G, Szalay A, Moser RD, Meneveau C (2016) A Web Services-accessible database of turbulent channel flow and its use for testing a new integral wall model for LES. *J Turbul* 17(2):181–215
- Huhn F, Schanz D, Gesemann S, Manovski P, Schröder A (2016) Pressure reconstruction from Lagrangian particle tracking with FFT integration. In: 18th international symposium on the application of laser and imaging techniques to fluid mechanics. Lisbon, Portugal, 4–7 July 2016

- Jeon YJ, Tronchin T, Chatellier L, David L (2014) 3D extension of the fluid trajectory evaluation based on an ensemble averaged cross-correlation (FTEE) for acceleration and pressure. In: 17th international symposium on applications of laser techniques to fluid mechanics. Lisbon, Portugal, 07–10 July 2014
- Jeon Y, Earl T, Braud P, Chatellier L, David L (2016) 3D pressure field around an inclined airfoil by tomographic TR-PIV and its comparison with direct pressure measurements. In: 18th international symposium on the application of laser and imaging techniques to fluid mechanics. Lisbon, Portugal, 4–7 July 2016
- Jimenez J, Hoyas S (2008) Turbulent fluctuations above the buffer layer of wall-bounded flows. *J Fluid Mech* 611:215–236
- Joshi P, Liu X, Katz J (2014) Effect of mean and fluctuating pressure gradients on boundary layer turbulence. *J Fluid Mech* 748:36–84
- Kim KC, Adrian RJ (1999) Very large-scale motion in the outer layer. *Phys Fluids* 11(2):417–422
- Kobashi Y, Ichijo M (1986) Wall pressure and its relation to turbulent structure of a boundary layer. *Exp Fluids* 4:49–55
- Lecordier B, Westerweel J (2004) The EUROPIV Synthetic Image Generator (S.I.G.). In: Proceedings of the EUROPIV 2 workshop, Zaragoza, Spain, 31 March–1 April 2003
- Lesieur M, Métais O (1996) New trends in large-eddy simulations of turbulence. *Ann Rev Fluid Mech* 28:45–82
- Li Y, Perlman E, Wan M, Yang Y, Burns R, Meneveau C, Burns R, Chen S, Szalay A, Eyink G (2008) A public turbulence database cluster and applications to study Lagrangian evolution of velocity increments in turbulence. *J Turbul* 9:1–29
- Liu X, Katz J (2006) Instantaneous pressure and material acceleration measurements using a four-exposure PIV system. *Exp Fluids* 41(2):227–240
- Liu X, Katz J (2008) Cavitation phenomena occurring due to interaction of shear layer vortices with the trailing corner of a two-dimensional open cavity. *Phys Fluids* 20(4):041702–041702
- Liu X, Katz J (2013) Vortex-corner interactions in a cavity shear layer elucidated by time-resolved measurements of the pressure field. *J Fluid Mech* 728:417–457
- Liu X, Katz J (2017) Pressure–rate-of-strain, pressure diffusion, and velocity–pressure-gradient tensor measurements in a cavity flow. In: 55th AIAA aerospace sciences meeting AIAA SciTech forum, Grapevine, Texas, 9–13 January 2017
- Liu S, Meneveau C, Katz J (1994) On the properties of similarity subgrid-scale models as deduced from measurements in a turbulent jet. *J Fluid Mech* 275:83–119
- Liu X, Moreto JR, Siddle-Mitchell S (2016) Instantaneous pressure reconstruction from measured pressure gradient using rotating parallel ray method. In: 54th AIAA aerospace sciences meeting, San Diego, California, USA, 4–8 January 2016
- Lynch K, Scarano F (2013) A high-order time-accurate interrogation method for time-resolved PIV. *Meas Sci Technol* 24:035305
- Lynch K, Scarano F (2014) Material acceleration estimation by four-pulse tomo-PIV. *Meas Sci Technol* 25:084005
- Morris MJ (1995) Use of pressure-sensitive paints in low speed flows. In: IEEE 16th International Congress on Instrumentation in Aerospace Simulation Facilities (ICIASF), Wright-Patterson AFB, OH, 18–21 July 1995
- Naka Y, Stanislas M, Foucaut J, Coudert S, Laval J, Obi S (2015) Space–time pressure–velocity correlations in a turbulent boundary layer. *J Fluid Mech* 771:624–675
- Neeteson N, Rival D (2015) Pressure-field extraction on unstructured flow data using a Voronoi tessellation-based networking algorithm: a proof-of-principle study. *Exp Fluids* 56:44–57
- Panton RL, Goldmann AL, Lowery RL, Reischman MM (1980) Low-frequency pressure fluctuations in axisymmetric turbulent boundary layers. *J Fluid Mech* 97:299–319
- Perlman E, Burns R, Li Y, Meneveau C (2007) Data exploration of turbulence simulations using a database cluster. In: Supercomputing SC07 ACM IEEE, Reno, NV, USA, 10–16 Nov. 2007
- Peterson JI, Fitzgerald VF (1980) New technique of surface flow visualization based on oxygen quenching of fluorescence. *Rev Sci Instrum* 51:670–671
- Pope SB (2000) Turbulent flows. Cambridge University Press, Cambridge
- Roache PJ (1976) Computational fluid dynamics, Hermosa Publ., Albuquerque, NM
- Rogallo R, Moin P (1984) Numerical simulation of turbulent flows. *Ann Rev Fluid Mech* 16:99–137
- Schanz D, Gesemann S, Schröder A (2016) Shake-the-box: Lagrangian particle tracking at high particle image densities. *Exp Fluids* 57:70–97
- Schneiders JFG, Pröbsting S, Dwight RP, van Oudheusden BW, Scarano F (2016) Pressure estimation from single-snapshot tomographic PIV in a turbulent boundary layer. *Exp Fluids* 57(4):–53
- Sexton MR, O'Brien WF, Moses HL (1973) An on Rotor Investigation of Rotating Stall in an Axial Compressor. Defense Technical Information Center (DTIC) Technical Report, Cameron Station, Alexandria, VA
- Sheng J, Malkiel E, Katz J (2006) Digital holographic microscope for measuring three-dimensional particle distributions and motions. *Applied optics* 45:3893–3901
- Spanier EH (1966) Algebraic topology. Springer, New York
- Stanislas M, Okamoto K, Kähler CJ, Westerweel J (2005) Main results of the second international PIV challenge. *Exp Fluids* 39:170–191
- Talapatra S, Katz J (2013) Three-dimensional velocity measurements in a roughness sublayer using microscopic digital inline holography and optical index matching. *Meas Sci Technol* 24:024004
- Tronchin T, David L, Farcy A (2015) Evaluation of pressure field and fluid forces for 3D flow around flapping wing. *Exp Fluids* 56:7–23
- Tsuji Y, Ishihara T (2003) Similarity scaling of pressure fluctuation in turbulence. *Phys Rev E* 68:026309
- Tsuji Y, Fransson JHM, Alfredsson PH, Johansson V (2007) Pressure statistics and their scaling in high-Reynolds-number turbulent boundary layers. *J Fluid Mech* 585:1–40
- van Oudheusden BW (2013) PIV-based pressure measurement. *Meas Sci Technol* 24(3):32001
- van Oudheusden BW, Scarano F, Roosenboom E, Casimir EWF, Souverein LJ (2007) Evaluation of integral forces and pressure fields from planar velocimetry data for incompressible and compressible flows. *Exp Fluids* 43:1–12
- van Gent LP, Michaelis D, van Oudheusden BW, Weiss PE, de Kat R, Laskari A, Jeon Y, David L, Schanz D, Huhn F, Gesemann S, Novara M, McPhaden C, Neeteson N, Rival DE, Schneiders JFG, Schrijer FFJ (2017) Comparative assessment of pressure field reconstructions from particle image velocimetry measurements and Lagrangian particle tracking. *Exp Fluids* 58:33–56
- Villegas A, Diez FJ (2014) Evaluation of unsteady pressure fields and forces in rotating airfoils from time-resolved PIV. *Exp Fluids* 55(4):1–17
- Violato D, Moore P, Scarano F (2011) Lagrangian and Eulerian pressure field evaluation of rod-airfoil flow from time-resolved tomographic PIV. *Exp Fluids* 50(4):1057–1070
- Willmarth WW (1975) Pressure Fluctuations Beneath Turbulent Boundary Layers. *Annu Rev Fluid Mech* 7:13–36

- Worth NA, Nickels TB, Swaminathan N (2010) A tomographic PIV resolution study based on homogeneous isotropic turbulence DNS data. *Exp Fluids* 49:637–656
- Yu H, Kanov K, Perlman E, Graham J, Frederix E, Burns R, Szalay A, Eyink G, Meneveau C (2012) Studying Lagrangian dynamics of turbulence using on-demand fluid particle tracking in a public turbulence database. *J Turbul* 13:1–29
- Zhang C, Miorini R, Katz J (2015) Integrating Mach–Zehnder interferometry with TPIV to measure the time-resolved deformation of a compliant wall along with the 3D velocity field in a turbulent channel flow. *Exp Fluids* 56:203–225
- Zhang C, Wang J, Blake W, Katz J (2017) Deformation of a compliant wall in a turbulent channel flow. *J Fluid Mech* 823:345–390

Publisher's Note Springer Nature remains neutral with regard to jurisdictional claims in published maps and institutional affiliations.